ADVANCED ENERGY MATERIALS
www.advenergymat.de

Continuous Production of Ethylene and Hydrogen Peroxide from Paired Electrochemical Carbon Dioxide Reduction and Water Oxidation

Sotirios Mavrikis, Matthian Nieuwoudt, Maximilian Göltz, Sophie Ehles, Andreas Körner, Andreas Hutzler, Emeric Fossy, Andreas Zervas, Oshioriamhe Brai, Moritz Wegener, Florian Doerrfuss, Peter Bouwman, Stefan Rosiwal, Ling Wang, and Carlos Ponce de León**

Paired electrolysis offers an auspicious strategy for the generation of high-value chemicals, at both the anode and cathode, in an integrated electrochemical reactor. Through efficient electron utilization, routine product misuse at overlooked electrodes can be prevented. Here, an original paired electrosynthetic system is reported that can convert CO_2 to ethylene (C_2H_4) at the cathode, and water to hydrogen peroxide (H_2O_2) at the anode under a single pass of electric charge. Amongst various investigated copper (Cu) nanomorphologies, the bespoke mixed Cu nanowire/nanoparticle catalyst recorded a peak C_2H_4 Faraday efficiency (*FE*) of 60% following 370 h of electrolysis at 200 mA cm^{-2}, while the tailored boron-doped diamond (BDD) anode accumulated an unprecedented ≈1% w/w of H_2O_2 in 4 M K_2CO_3 upon applying 300 mA cm^{-2} for 10 h. When paired, the dual C_2H_4-H_2O_2 electrochemical cell attains a combined *FE* of 120% for 50 h at 200 mA cm^{-2}, a combined energy efficiency (EE) of 69%, and a 50% decrease in the overall electrical energy consumption (EEC) compared to the individual electrosynthesis of C_2H_4 and H_2O_2.

1. Introduction

Prominent aqueous electrochemical processes such as carbon dioxide (CO_2) reduction toward hydrocarbons and alcohols, or water reduction to H_2, and N_2 reduction to NH_3, allow for the electrogeneration of valuable organic and inorganic commodities at the cathode, while the anodic reaction, typically oxygen evolution, is routinely disregarded.[1] Paired electrolysis permits the practical electrochemical production of such nexus chemicals at both electrodes with minimal waste and by-product generation, whilst also cutting costs, saving resources and maximizing the energy efficiency and atom economy of the combined system.[2–5]

The twelve-electron CO_2 reduction reaction (12e^- CO_2RR) has hastily garnered

S. Mavrikis, M. Nieuwoudt, S. Ehles, E. Fossy, O. Brai, C. Ponce de León
Electrochemical Engineering Laboratory
Energy Technology Research Group
Faculty of Engineering and Physical Sciences
University of Southampton Highfield Campus
University Road, Southampton SO17 1BJ, UK
E-mail: s.mavrikis@soton.ac.uk; capla@soton.ac.uk

S. Mavrikis, L. Wang
National Centre for Advanced Tribology at Southampton (nCATS)
Faculty of Engineering and Physical Sciences
University of Southampton Highfield Campus
University Road, Southampton SO17 1BJ, UK

M. Göltz, S. Rosiwal
Chair of Materials Science and Engineering for Metals
Faculty of Engineering
Friedrich-Alexander-Universität Erlangen-Nürnberg
91058 Erlangen, Germany

A. Körner, A. Hutzler
Forschungszentrum Jülich GmbH
Helmholtz Institute Erlangen-Nürnberg for Renewable Energy (IEK-11)
Cauerstraße 1, 91058 Erlangen, Germany

A. Zervas
Department of Civil Engineering
University of Patras
Patras 26500, Greece

M. Wegener, F. Doerrfuss, P. Bouwman
Schaeffler Technologies AG & Co. KG
Industriestraße 1–3, 91074 Herzogenaurach, Germany

The ORCID identification number(s) for the author(s) of this article can be found under https://doi.org/10.1002/aenm.202304247

DOI: 10.1002/aenm.202304247

widespread attention as an appealing method for the electrochemical synthesis of ethylene (C_2H_4), the most commonly-produced organic compound in the world, with a range of industrial applications including the large-scale production of ethylene oxide, ethylene glycol and polyethylene.[6] State-of-the-art copper (Cu) coated gas diffusion electrodes (GDEs) have shown great promise for the formation of multi hydrocarbon (C_{2+}) species,[7,8] however major bottlenecks of this concept include selectivity toward C_2H_4 (with the hydrogen evolution reaction, HER, being the predominant competing reaction, alongside CO generation),[9,10] and the instability of the GDE due to catalyst delamination and flooding of the diffusion layer.[11–15] The two-electron water oxidation reaction ($2e^-$ WOR) is an unconventional yet propitious route for the electrochemical production of hydrogen peroxide (H_2O_2), instead of oxygen, at the anode.[16] Despite not being as established as the popular two-electron oxygen reduction reaction ($2e^-$ ORR), notable advancements have been made with respect to catalyst design and the current efficiency for H_2O_2 electrosynthesis.[17,18] Practical limitations of the $2e^-$ WOR, however, include inadequate H_2O_2 output concentrations, low operational current densities, the stability of the anode, and an overwhelming majority of investigations carried out in laboratory-scale H-type batch cells, instead of industrially-relevant and larger (pertaining to the active area of the catalyst) flow reactors.

The feasibility of exploiting the anode, during the highly-coveted electrochemical conversion of CO_2 toward C_2H_4, to produce valuable and versatile chemicals like H_2O_2, instead of oxygen, has, to date, not been investigated.[19–22] Consequently, in this work, upon optimization of each respective process separately, the $12e^-$ CO_2RR is coupled with the $2e^-$ WOR for the first time, resulting in the assembly of an electrochemical flow reactor where the in situ parallel dual electrosynthesis of C_2H_4 (at a Cu/GDE cathode) and H_2O_2 (at a boron-doped diamond, BDD, anode) is achieved simultaneously at a cell voltage of 4.99 V. This promptly effectuates a combined energy efficiency (EE) of 69%, alongside a 50% lower electrical energy consumption (EEC) of 11.77 kWh $kg^{-1}_{Products}$ and a combined Faraday efficiency of 120% under an applied current density of 200 mA cm^{-2} for 50 h of continuous paired electrolysis. A preliminary technoeconomic evaluation of the combined electrolytic $12e^-$ CO_2RR/$2e^-$ WOR system showcases an estimated 42% increase in the added value (AV), as well as a positive AV of €0.18 $kg^{-1}_{Products}$ of the paired electrosynthesis products (C_2H_4 and H_2O_2), compared to the non-paired ones electrochemical process. The concepts developed, as well as the results attained, within this work can be incorporated in a future scaled up system where further nonelectrochemical transformations can be realized, such as the chemical production of ethylene oxide (C_2H_4O) from electrosynthesized C_2H_4 and H_2O_2.

2. Results and Discussion

2.1. Bespoke $12e^-$ CO_2RR and $2e^-$ WOR Catalyst Characterization

A comprehensive characterization of the cathodic material introduced for the $12e^-$ CO_2RR measurements carried out in this work is presented in **Figure 1**. The self-ordered and moderately natural agglomeration of the mixed Cu nanowire/nanoparticle catalyst deployed on the microporous layer of the GDE, for the $12e^-$ CO_2RR, can be seen in the top view (Figure 1a), broken cross-section (Figure 1b) and ion-mill-polished cross-section (Figure 1c) SEM images. For easier differentiation of the GDE layers in Figure 1c, the Cu nanowires are artificially colored yellow, the Cu nanoparticles orange, the fibrous carbon substrate grey, and the conductive varnish for SEM imaging in violet. Consequently, it is observed that the Cu nanowires generally do not infiltrate the finer pores of the rough carbon fibers, but instead generate a weblike network on its surface, spanning larger crevices as seen in the centre of Figure 1b,c,g. The latter laser scanning microscopy (LSM) mapping showcases the frequency and depth of these cracks, commonly ≥ 50 µm, and that some of them are overlaid and only emerge lightly, as confirmed by further SEM images in the Supporting Information, revealing that the Cu nanowire network interlines or bridges these apertures (Figures S1–S4, Supporting Information). The Cu nanowire network additionally appears mechanically stable (at breaking edges), forming freestanding lamellae as seen in Figure 1b. In contrast to the Cu nanowires, the Cu nanoparticles were embedded both in the Cu network (up to ≈2 µm thick) and within the GDL (infiltration in pores up to ≈5 µm deep). In positions where only Cu particles, primarily Cu nanocubes, were present at the fibrous carbon surface, such as within the pores depicted in Figure 1c, the deposited Cu layer measures 200 nm in thickness?

An average edge length of 69 nm (σ = 14 nm) has been determined for the Cu nanocubes and an average diameter of 48 nm (σ = 12 nm) is measured for the Cu nanowires, as portrayed in Figure 1d,h,j. The chemical composition of the mixed Cu catalyst is evaluated by STEM-EDXS and confirmed to be metallic copper (Figure 1e), with minor signals for oxygen (Figure 1f), likely originating from the surface oxidation of a few atomic layers post-electrolysis since the material was not hermetically sealed and thus susceptible to air and humidity. This is further confirmed by SAED analysis (Figure 1i). The Cu nanocubes were oriented in {200} while the wires grow along the {110} axis (Figure 1h–k) as has been reported.[23–25] The determination of the lattice distance can be found in Figures S5–S9 (Supporting Information).

XPS analysis of the Cu mixed catalyst surface reveals standard carbon contamination, an oxygen O 1s peak and various copper signals (Figure 1l). The Cu 2p region displays distinct peaks for metallic copper and various oxidized copper states like Cu_2O, CuO and $Cu(OH)_2$. XRD measurements (Figure 1m) further support the assumption of superficial oxides due to air exposure with signals recorded from plain C-paper (violet), C-paper coated with the Cu mixed catalyst (orange), and their difference (blue). In the latter, all signals from the substrate were eliminated and the four remaining peaks at 43.3°, 50.4°, 74.1°, and 90° agree with the expected diffraction signals for metallic face-centred cubic (FCC) copper, of the {111}, {200}, {311}, and {222} planes, respectively (JCPDS file no. 03–1018).[26]

Three boron doped diamond (BDD) coatings, deposited on 1 mm thick niobium plates (Figure S10, Supporting Information) for the $2e^-$ WOR in an electrochemical flow reactor, denoted BDD-a, BDD-b and BDD-c (Table S1, Supporting Information), respectively, were synthesized in a custom-built hot filament CVD apparatus as described previously.[27] The boron doping levels, quantified by GDOES, have been adjusted to 12600 ppm for BDD-a, and to ≈20000 ppm for BDD-b and BDD-c. Concerning

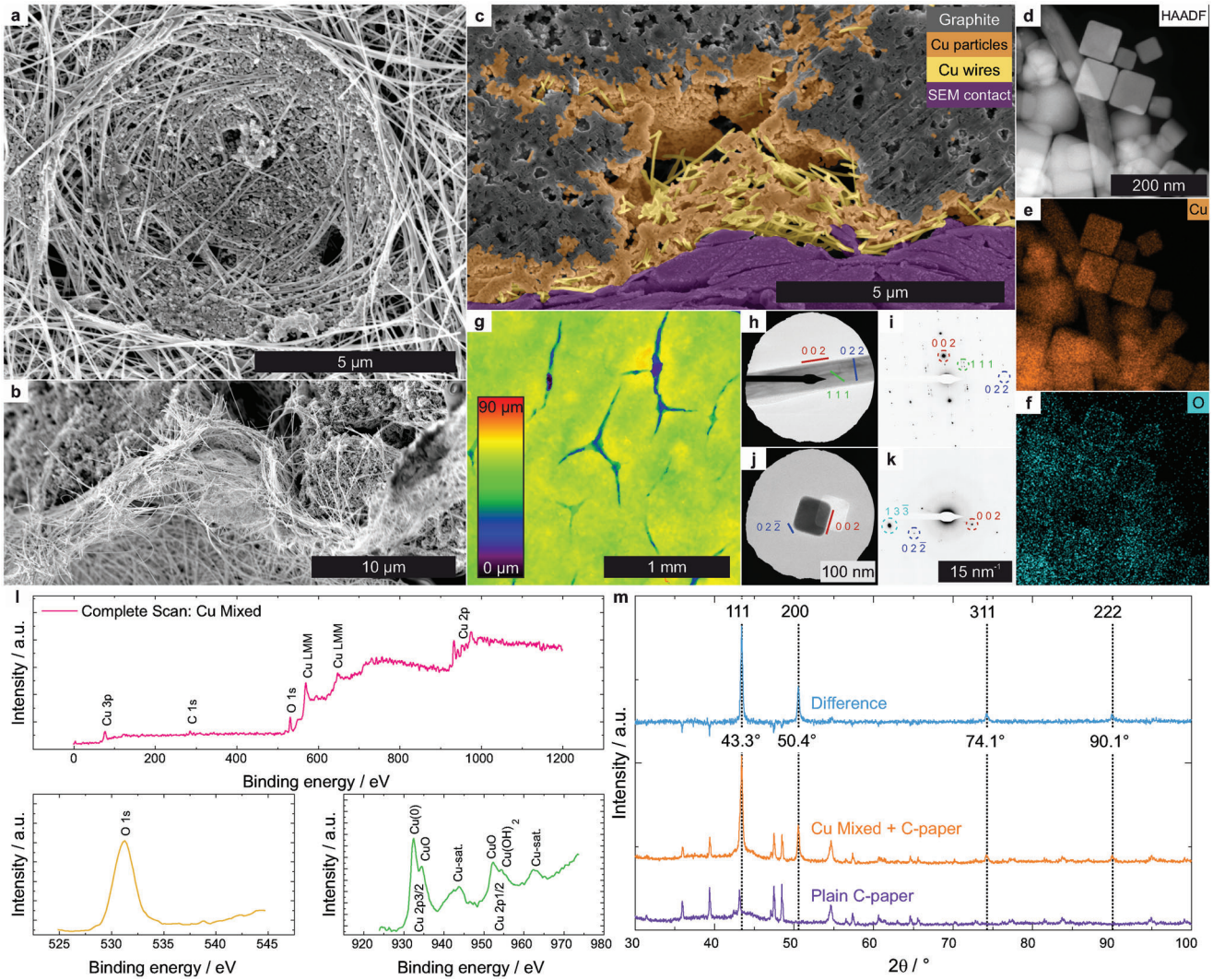

Figure 1. Structural characterization of the novel 12e^- CO_2RR electrocatalyst used in this work. a) Top view SEM micrograph of the mixed copper nanowire/nanoparticle electrocatalyst, scale bar: 5 µm. b) SEM micrograph of a broken cross section SEM of the Mixed Cu/GDE, scale bar: 10 µm. c) Ion-mill polished cross section SEM (artificially colored) of the Mixed Cu/GDE, scale bar: 5 µm. d) STEM-HAADF analysis of the Mixed Cu catalyst suspended in toluene, scale bar: 200 nm. e) STEM-EDXS analysis of the Mixed catalyst for Cu distribution. f) STEM-EDXS analysis of the mixed catalyst for O distribution. g) LSM scan of the Mixed Cu-coated Vulcan GDE, scale bar: 1 mm. h) SAED of single Cu-wire-Cu lattice planes marked, scale bar: 100 nm. i) SAED-diffraction image of SAED of single Cu-wire-Cu lattice planes marked, scale bar: 15 nm^{-1}. j) SAED of single Cu-cube-Cu lattice planes marked, scale bar: 100 nm. k) SAED-diffraction image of single Cu-cube-Cu lattice planes marked, scale bar: 15 nm^{-1}. l) XPS analysis showing Cu, C and O signals (the Cu 2p region contains signals of both metallic and Cu oxide). m) XRD spectra of Mixed Cu/GDE (orange), plain/uncoated GDE background (violet) and the remaining catalyst signal (blue).

the surface of the three variants, SEM micrographs (**Figure** 2a–c) disclose that BDD-a and BDD-b possess an average facet size of 0.47 and 0.48 nm, respectively, while BDD-c averages 0.91 nm. The diamond coating thickness measures at 1.6, 1.6 and 3.1 µm, for BDD-a, BDD-b and BDD-c, respectively, while a microcrystalline morphology is uniformly spread across the niobium substrate with an overall roughness (Rz) between 3 and 5 µm (Figure 2d; Figure S11, Supporting Information). EBSD analysis (Figure 2e; Figure S12, Supporting Information) of the cross section in Figure 2f confirms that the BDD morphology is polycrystalline with a predominant occurrence of {111} and {101} facets. XRD analysis (Figure 2g) further corroborates that the diamond peaks exhibit a typical distribution for this morphology (JCPDS file no. 06–0675),[28] while unmarked peaks were attributed to Nb or NbC of the substrate. In the Raman spectra of the diamond films, the sp^3-carbon peak at 1332 cm^{-1} is tilted to the left and overlayed by the signal at 1230 cm^{-1} (Figure 2h) due to boron doping. This phenomenon, coupled with the pronounced band at 500 cm^{-1}, is associated with a high level of boron doping, and is notably stronger for films BDD-b and BDD-c, whose sp^2-carbon bands at ≈1500 cm^{-1} were concealed. The same bands remain visible for BDD-a, which possesses a lower boron doping level.[27]

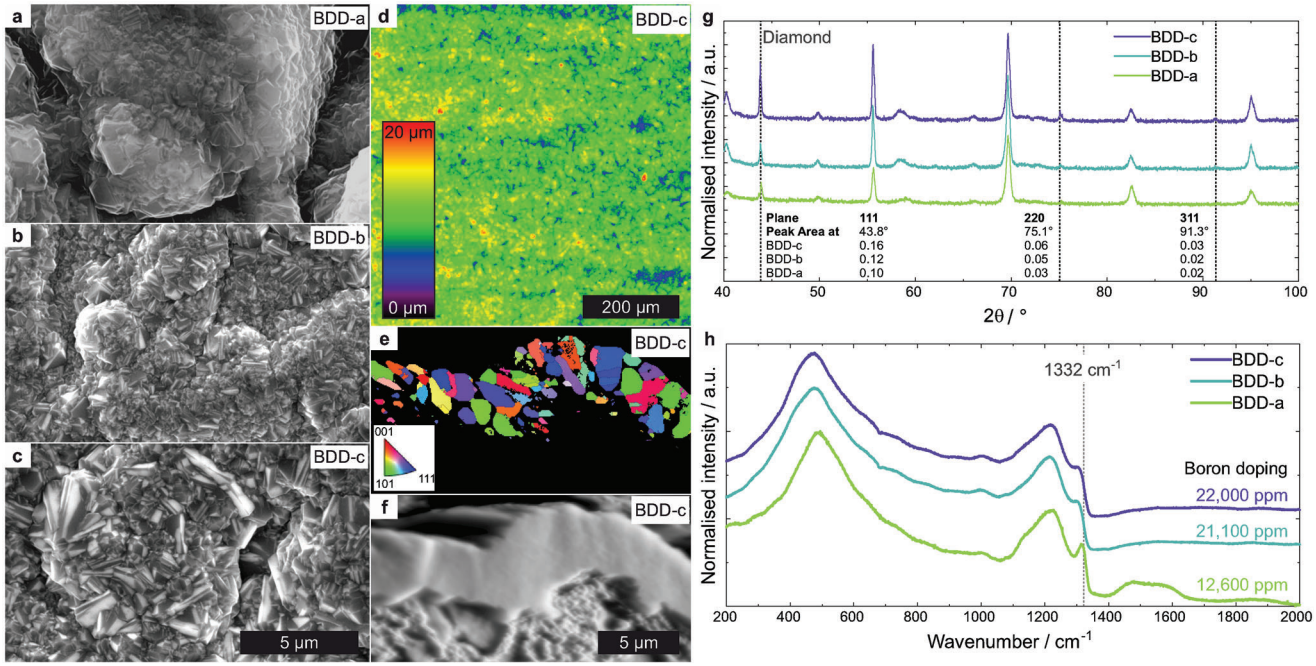

Figure 2. Structural characterization of the $2e^-$ WOR electrocatalysts used in this work. a) SEM micrograph of the crystal morphology of BDD-a (facet size: 0.467 µm; boron doping: 12600 ppm), scale bar: 5 µm. b) SEM micrograph of the crystal morphology of BDD-b (facet size: 0.487 µm; boron doping: 22000 ppm), scale bar: 5 µm. c) SEM micrograph of the crystal morphology of BDD-c (facet size: 0.908 µm; boron doping: 12600 ppm), scale bar: 5 µm. d) LSM scan of the surface morphology of BDD-c, scale bar: 200 µm. e) EBSD scan of BDD-c demonstrating a polycrystalline structure with mostly {111} and {101} facets, scale bar: 5 µm. f) FSD image of the EBSD scan of BDD-c, scale bar: 5 µm. g) XRD analysis of BDD-a, BDD-b and BDD-c exhibiting peaks for {111}, {220} and {311}, Nb and NbC. h) Raman spectra of BDD-a, BDD-b and BDD-c with the sp^3-carbon (diamond) signal at 1332 cm^{-1} visible but tilted by boron incorporation.

2.2. Optimized Electrocatalytic $12e^-$ CO_2RR

Using the mixed copper electrocatalyst (optimal loading 1 mg cm^{-2}; Figure S13, Supporting Information) in five different combinations of substrate (Figures S14 and S15, Supporting Information) and PTFE pre-treatment (Tables S2 and S3, Supporting Information), the electrocatalytic capability of the bespoke GDEs to produce C_2H_4 was investigated in an H-cell for 2 h under a constant current density of 150 mA cm^{-2} in 1 M KOH (**Figure 3a**). Of the five GDEs evaluated, Mixed-1 recorded an average appt. *FE* of 48% throughout the duration of electrolysis likely due to hydrophobic pre-treatment of the macro and microporous layers as well as the excellent (observed) adhesion of the mixed Cu electrocatalyst to the Vulcan carbon particles, without the use of a binder. In contrast, mixed-2 exhibits a lower C_2H_4 electrosynthesis performance (and a higher selectivity toward CH_4 —Figure S16, Supporting Information) which could be attributed to the inclusion of PTFE in the catalyst ink (prior to coating), hindering the diffusion of CO_2 to the catalyst surface, lowering the overall conductivity of the GDE or rendering fewer active sites available for C_2H_4 production.[9] Next, to assess the performance of the mixed Cu catalyst to electrochemically convert CO_2 to C_2H_4, several of the most prominent Cu catalyst morphologies reported in the $12e^-$ CO_2RR literature were prepared in house,[29,30] coated on the Vulcan substrate (Table S4, Supporting Information), and evaluated under identical operating conditions (see Experimental Section). As seen in Figure 3b, the bespoke mixed GDE exhibited an impressive C_2H_4 accumulation ability, attaining an apparent (appt.) *FE* of 49% at 200 mA cm^{-2} and maintaining an appt. *FE* above 40% at 300 mA cm^{-2}, whereas the other Cu nano-catalyst GDEs were unable to reach an appt *FE* of 40%. The superior C_2H_4 electrocatalytic capability of the bespoke mixed Cu nanowire/nanoparticle catalyst, compared to the other Cu morphologies (Figure S17, Supporting Information), can likely be attributed to a synergistic effect amongst the nanowire and nanoparticle morphologies, emerging from their different geometries. It is observed that the Cu nanowires form a second nano porous layer upon the Vulcan-based GDL, vaguely reminiscent of a copper "nano felt" (Figures S1–S4, Supporting Information), that can bridge the larger crevices within the GDL surface, exhibiting excellent adhesion to the Vulcan-based GDL as well as noteworthy mechanical strength. The smaller Cu nanoparticles infiltrate the finer pore networks of the GDL, and additionally occupy the Cu nano felt formed by the Cu nanowires. The strong adhesion of the Cu nano felt to the Vulcan GDL, and of the Cu nanoparticles to the Cu nanowires, both render the utilization of a binder superfluous. The additional 3D catalyst loading capacity of the GDE substantially increases the amount of active material per geometric surface area, likely allowing for higher *FE*s at larger current densities. The 3D loading capacity permits the Cu catalyst to trap and interact with CO_2 constantly flowing through the larger and spanned cracks within the GDL that would otherwise leave the cathode with no contact with the Cu catalyst at any point. The Cu nanowires also aid lateral and vertical conductivity by way of connecting the

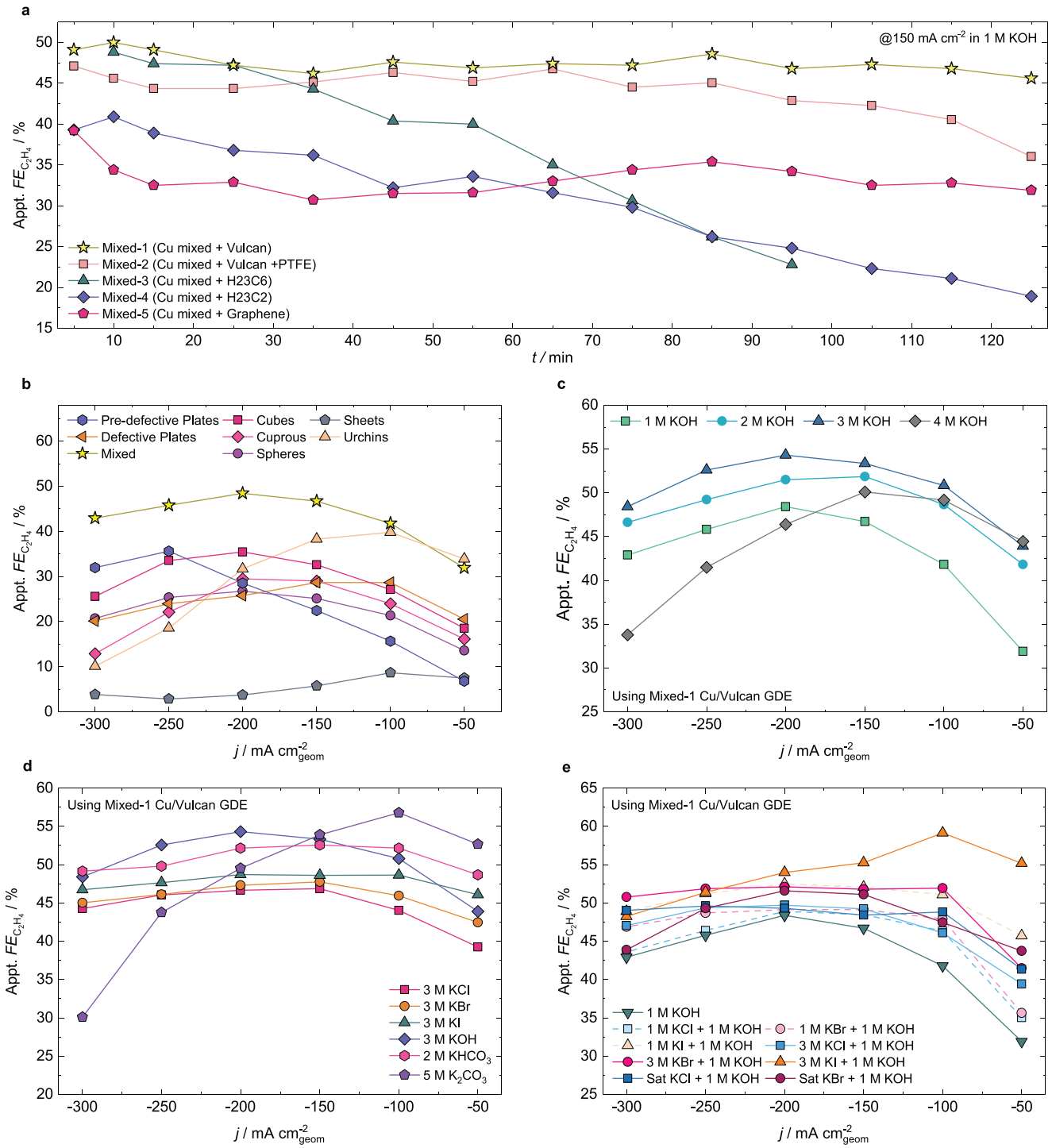

Figure 3. Electrocatalytic $12e^-$ CO_2RR screening measurements using bespoke copper-based GDEs in an H-type cell. a) Apparent (Appt.) C_2H_4 faradaic efficiency during a two-hour continuous chronopotentiometry measurement at 150 mA cm^{-2} in 1 M KOH using the mixed Cu electrocatalyst loaded on different carbon-based substrates (see Table S3, Supporting Information). b) Appt. C_2H_4 faradaic efficiency from the screening of the $12e^-$ CO_2RR electrocatalytic performance of various Cu based catalysts, loaded onto a Vulcan XC 72R/Sigracet SGL 28 BC support, in 1 M KOH within an applied current density range of 50–300 mA cm^{-2} (increments of 50 mA cm^{-2}; electrolysis duration: 5 min at each current). c) Appt. C_2H_4 faradaic efficiency of the Mixed-1 GDE in different KOH solutions plotted as a function of the applied current. d) Appt. C_2H_4 faradaic efficiency of the mixed-1 GDE in different concentrated potassium-based aqueous solutions versus the applied current. e) Appt. C_2H_4 faradaic efficiency of the mixed-1 GDE in different concentrated potassium-based aqueous solutions versus the applied current.

incorporated Cu nanoparticles to the source of electrical energy, the GDE surface, minimizing the ohmic drop within the GDE. The electrical conductivity of the GDE is also enhanced by the lack of a binder in the Cu catalyst ink.

In an attempt to further suppress the HER and minimize ohmic losses, four different concentrations of KOH (1–4 M) were evaluated in standard H-cell conditions using the Mixed-1 electrode (Figure 3c). Upon doubling (2 M) and tripling (3 M) the catholyte concentration, a notable increase in the appt. *FE* for C_2H_4 production is observed, with a peak appt. *FE* of 54.4% reached at 200 mA cm^{-2} in 3 M KOH. Interestingly, increasing the KOH concentration to 4 M results in an overall diminished performance (Figure S18, Supporting Information), with the appt. *FE* peaking at 150 mA cm^{-2} (50.1%), before rapidly dropping to below 35%, contradicting prior studies which have reported enhanced C_2H_4 *FE*s in KOH concentrations of up to 10 M.[31,32] The performance of mixed-1 was additionally determined in several concentrated potassium-based aqueous electrolytes (Figure S19, Supporting Information), with pH values ranging between neutral and alkaline (Table S5, Supporting Information). The carbonate-based solution (5 M K_2CO_3) exhibited the highest selectivity toward C_2H_4 at lower currents (57%, 100 mA cm^{-2}) before rapidly declining to 30% at 300 mA cm^{-2} (Figure 3d). Bicarbonate-based solutions (2 M $KHCO_3$) displayed a constant appt. *FE* of 50–52% throughout the duration of electrolysis, while 3 M KOH, reaches peak appt. *FE*s (53–54%) between 200 and 250 mA cm^{-2}, with an overall lower overpotential for the $12e^-$ CO_2RR. Of the potassium halides salts assessed, 3 M KI attained the highest appt. *FE* of 48.75%, maintaining that value throughout the duration of electrolysis. Finally, electrolyte engineering (Figures S20–S24, Supporting Information) was employed to identify the optimal catholyte composition for maximal C_2H_4 accumulation during electrochemical CO_2 reduction (Table S5, Supporting Information). The addition of potassium halide salts in a standard 1 M KOH solution improved C_2H_4 electrosynthesis in all the tests carried out (Figure 3e) under standard H-cell conditions, resulting in a percentage increase of up to 17% apart from 3 M KI/1 M KOH, which reached a maximum appt. *FE* of 59.23% at 100 mA cm^{-2}, a 43% percentage increase compared to plain 1 M KOH. This observed $12e^-$ CO_2RR performance augmentation in our engineered KI/KOH mixture may be attributed to enhanced *CO adsorption and population at the surface of the mixed Cu catalyst,[33,34] likely stimulated by the synergistic co-adsorption of the I^- anion, resulting in ameliorated C—C coupling.[35,36]

Upon identifying the optimal Cu catalyst (mixed Cu), GDL (Vulcan-based) and electrolyte (KOH/KI) combination for enhanced C_2H_4 electrosynthesis via CO_2RR in an H-cell, a divided flow reactor (**Figure 4a**) was assembled with a 10 cm^2 cathode to evaluate the performance of the GDE under flow conditions. First, electrolyte screening measurements were carried out at a current range of 0.1–0.8 A cm^{-2} (Figure S25, Supporting Information) to determine an ideal KOH/KI molar ratio as well as the applied current value upon which the apparent *FE* for C_2H_4 was highest. As seen in Figure 4b it was found that a molar ratio of 1 M KOH/2 M KI reached a maximum appt. *FE* of 60% at 0.2 A cm^{-2} and maintained an appt. *FE* above 40% up to 0.7 A cm^{-2}. Consequently, a prolonged cumulative C_2H_4 electrosynthesis measurement was carried out at an applied current of 0.2 A cm^{-2} (Figure 4c) in 1 M KOH/2 M KI for 370 h of chronopotentiometry under single pass flow conditions. The mixed-1 GDE exhibited a remarkable stability over 370 h of electrolysis maintaining a constant cell voltage of 4.2 V (Figure 4d) at an applied current of 0.2 A cm^{-2}, corresponding to a specific electrical energy consumption (EEC) of 84.8 kWh $kg^{-1}{}_{C2H4}$, notably higher than the 7.5 kWh $kg^{-1}{}_{C2H4}$ required for hydrocarbon steam cracking.[37] With respect to gaseous product distribution our ECO_2RR system achieved a constant appt. *FE* of 60% for C_2H_4 production, 35% and 4% for H_2 and CO evolution, respectively, and additionally generated CH_4 at *FE*s below 1% over 370 h at 0.2 A cm^{-2} (Figure 4f). The attained C_2H_4 *FE* (60%), cell voltage (4.2 V), stability (370 h) and peak current density (800 mA cm^{-2}) values achieved in this electrochemical arrangement using mixed-1 are amongst the most notable in the $12e^-$ CO_2RR literature (Table S6, Supporting Information), particularly with respect to the larger-than-typical area of the mixed/Vulcan GDE (10 cm^2 for mixed-1 vs. 1 cm^2 for most GDEs), demonstrating the scalability and versatility of the bespoke mixed Cu nanowire/nanoparticle catalyst.

2.3. Electrocatalytic $2e^-$ WOR Under Flow Conditions

The $2e^-$ WOR electrocatalytic performance of BDD-a, the most active of the BDD films developed for this research (Figures S26 and S27, Supporting Information), to generate H_2O_2, is evaluated in a two-compartment, two-reservoir and two-electrode flow electrolyser (**Figure 5a**) using several carbonate-based aqueous electrolytes under recirculation flow conditions (400 mL min^{-1}) within an applied electrical current range of 100–1000 mA cm^{-2}. The composition and key properties of each assessed anolyte can be found in Table S7 (Supporting Information). In 2 KM K_2CO_3, 3.5 M of the "optimized (3.5 M K_2CO_3/0.5 M $KHCO_3$)" electrolyte and 4 M K_2CO_3, large current densities of up to 1 A cm^{-2} were recorded at average cell voltages of 8–9.5 V (Figure 5b), while the respective cell voltages recorded in 1 M K_2CO_3, and 2 M of the "hybrid (2 M K_2CO_3/2 M $KHCO_3$)" solution were already quite elevated at applied currents of 700–800 mA cm^{-2}. The concentration of H_2O_2 accumulated in the evaluated solutions increased proportionally to the increase in the applied current, with maximum values of 0.11, 0.116 and 0.12 M H_2O_2 (0.42–0.45% w/w H_2O_2) attained in 2 M K_2CO_3, 3.5 M "optimized" and 4 M K_2CO_3 (Figure 5c), thus accentuating the notable positive (redox) catalytic role of the carbonate ion ($CO_3{}^{2-}$) on anodic H_2O_2 electrosynthesis.[27,38–40] This notable influence of $CO_3{}^{2-}$ in H_2O_2 accumulation is further highlighted when quantifying the faradaic efficiency (appt. *FE*) for H_2O_2 production (Figure 5d), in which the *FE* peaks at 63% under an applied current of 300 mA cm^{-2} when 4 M K_2CO_3 is used as an electrolyte, compared to 60.9%, 57.55%, 56.1% and 48.4% for 2 M "hybrid", 3.5 M "optimized", 2 M K_2CO_3 and 1 M K_2CO_3, respectively, at the same applied current density. The gradual decay in the again appt. *FE* can be attributed to elevated OER as the applied current increases,[41] as well as further electrochemical oxidation of generated H_2O_2 under recirculation flow conditions. The H_2O—H_2O_2 partial current density of BDD-a gradually increases as the applied current increases, reaching a maximum value of 425 mA $cm^{-2}{}_{geom}$,

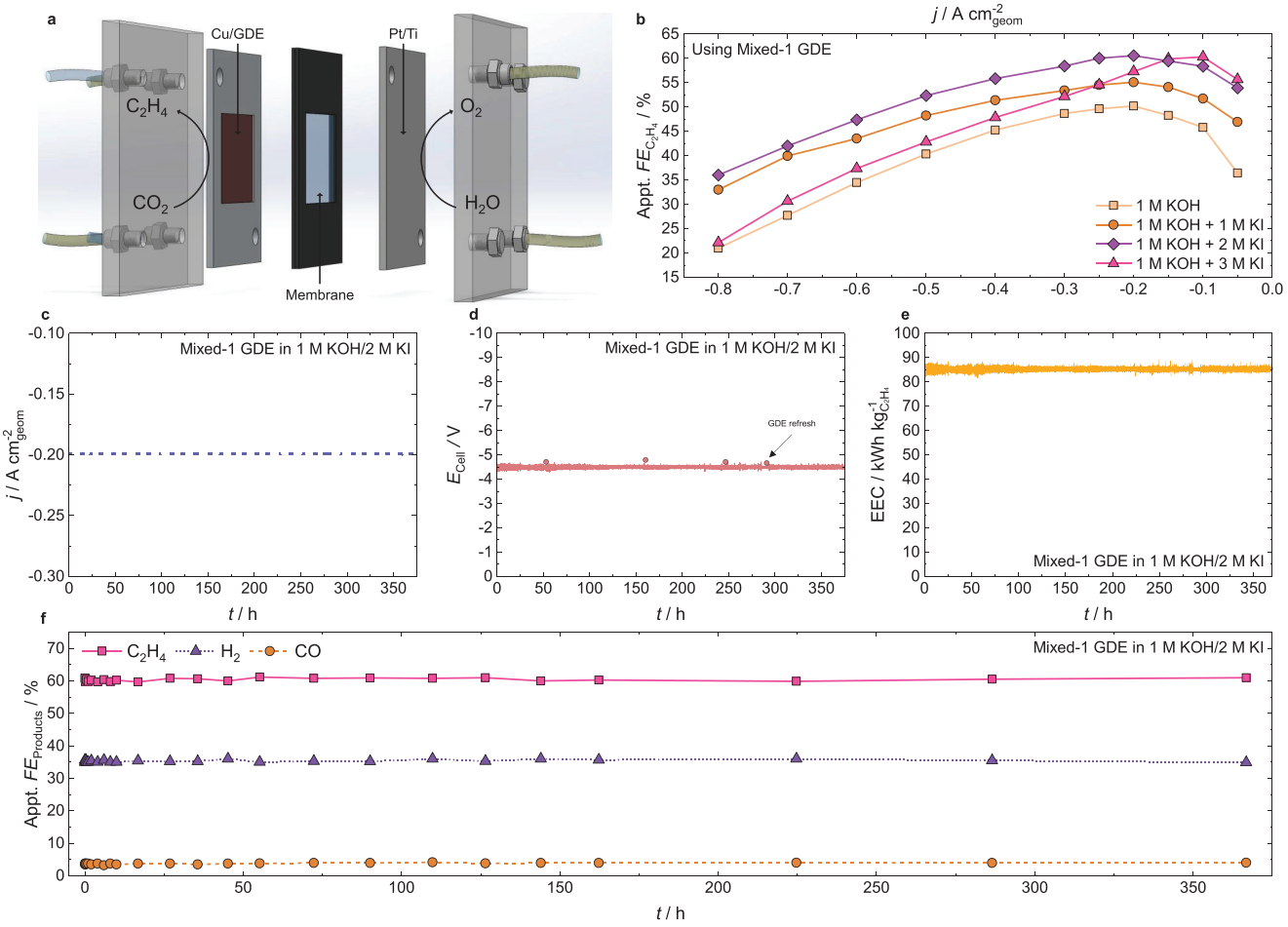

Figure 4. Prolonged C_2H_4 electrosynthesis measurement carried out in an electrochemical flow reactor. a) Simplified 3D schematic of the key components of the customized ElectroCell electrochemical flow reactor that can generate C_2H_4 via the $12e^-$ CO_2RR using a Cu-coated GDE. A detailed exploded-view diagram of the flow reactor can be seen in Figure S33 (Supporting Information). b) Appt. C_2H_4 faradaic efficiency of the mixed-1 GDE in different KOH/KI solutions as a function of the applied current (0.1–0.8 A cm^{-2}; increments of 0.1 A cm^{-2}; electrolysis duration: 5 min at each applied current). c) Applied electrical current versus time. d) Recorded total cell voltage plotted as a function of time. e) Calculated electrical energy consumption (EEC) plotted as a function of time. f) Appt. faradaic efficiency of the gaseous products (orange circles: CO; purple triangles: H_2; pink squares: C_2H_4) formed during a 370-h cumulative chronopotentiometry (0.2 A cm^{-2}) stability measurement in 1 M KOH/2 M KI using the bespoke mixed-1 GDE, which was replaced periodically.

corresponding to an initial (within the first 5 min of electrolysis) H_2O_2 production rate of 135 μmol cm^{-2} min^{-1}, in 4 M K_2CO_3, at a cell voltage of 9 V (Figure 5e), markedly the largest H_2O_2 production rate amongst the current existing $2e^-$ WOR electrocatalysts (Table S8, Supporting Information).[42–46] The $2e^-$ WOR performance of BDD-a in the 3.5 M "optimized" solution is also quite notable ($j_{Partial}$ 400 mA cm^{-2}_{geom}; int. H_2O_2 production rate 127 μmol cm^{-2} min^{-1}), albeit at a slightly higher cell voltage (9.5 V) upon the application of a total electric current of 1000 mA cm^{-2}_{geom}.

The long-term H_2O_2 electrosynthesis capability of BDD-a is further evaluated at a constant applied current of 300 mA cm^{-2} (**Figure 6a**), where the maximum appt. *FE* of 63% was attained, in plain 4 M K_2CO_3, as well as different 4 M K_2CO_3 solutions containing 4 and 8 g L^{-1} of sodium metasilicate (Na_2SiO_3), respectively, a known peroxy-species stabilizer,[47] for 10 h under continuous recirculation flow conditions. The BDD-a anode exhibited an impressive stability maintaining a fairly constant cell voltage of ≈6 V in all three electrolytes (Figure 6b), though fewer oxygen bubbles were observed in the mixtures containing Na_2SiO_3, likely due to its ability to slightly curtail H_2O_2 electrooxidation toward O_2. This phenomenon is further evident when observing the accumulation of H_2O_2 over time in the three solutions; within 6 h of electrolysis the concentration of H_2O_2 plateaus at ≈120 mM (0.45% w/w) in 4 M K_2CO_3, 175 mM (0.66% w/w) in 4 M K_2CO_3 containing 4 g L^{-1} Na_2SiO_3, and an unprecedented, for the $2e^-$ WOR, 250 mM (0.94% w/w) in 4 M K_2CO_3 containing 8 g L^{-1} Na_2SiO_3 (Figure 6c). Contrastingly, the appt. *FE* for H_2O_2 accumulation gradually decreases over time under recirculation galvanostatic flow due to the predominance of the OER, competitive H_2O_2 electrooxidation to O_2 and natural H_2O_2 disproportionation,[48] though this *FE* decay is markedly hindered in 4 M K_2CO_3 containing 8 g L^{-1} Na_2SiO_3 (Figure 6d) compared to the other two mixtures.

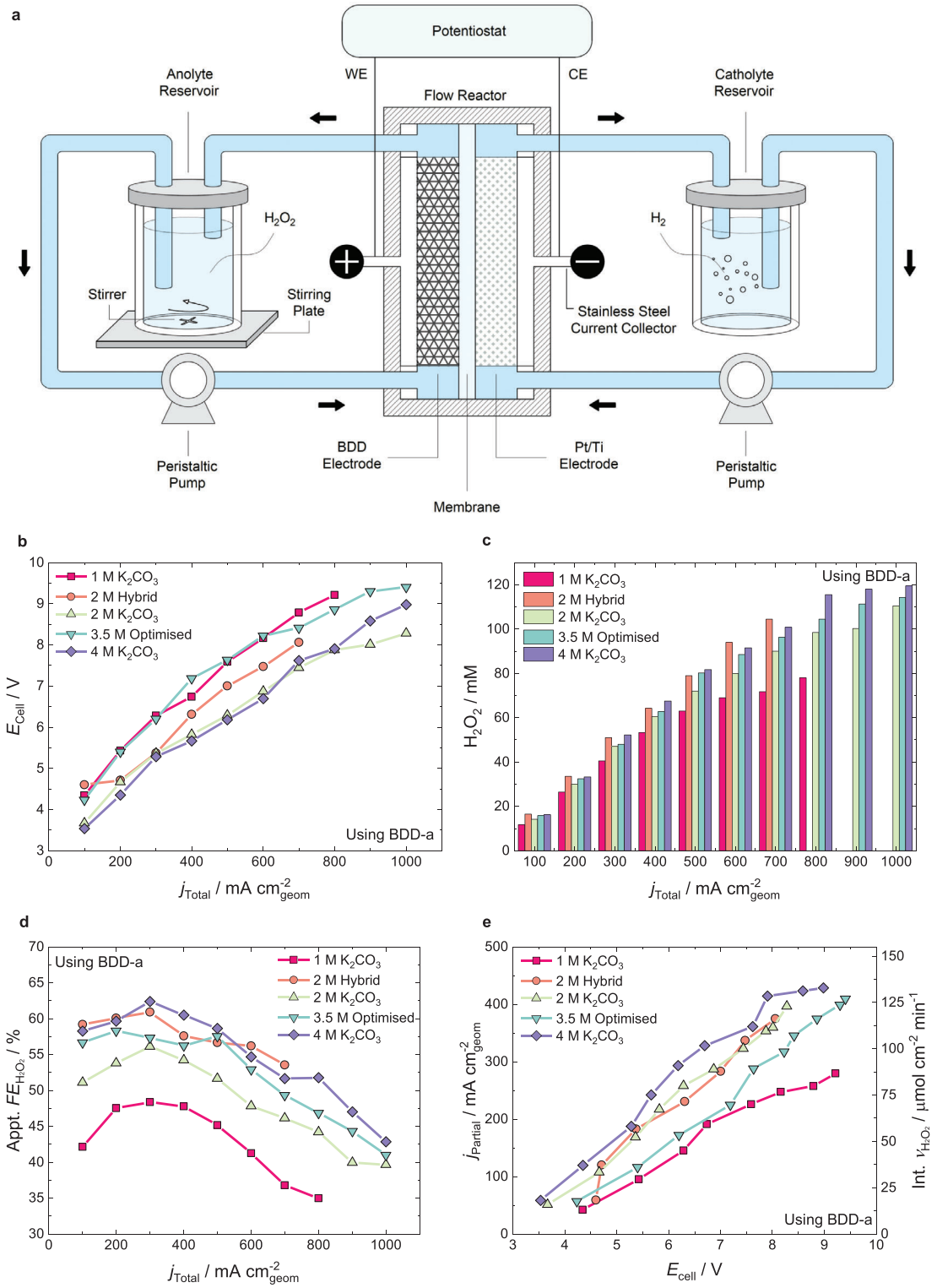

Figure 5. Electrolyte screening for the $2e^-$ WOR using BDD-a in a custom-made flow reactor with an electrolyte flow rate of 400 mL min^{-1}. a) Schematic diagram of the experimental setup used to electrochemically produce H_2O_2 via water oxidation, using BDD-a, under recirculation and galvanostatic flow conditions. b) Average cell voltage plotted as a function of the applied current density (range: 0–1000 mA cm^{-2}; increments of 100 mA cm^{-2}; electrolysis duration: 5 min for each current; fresh solution used for each individual experiment) using BDD-a in five different potassium carbonate and bicarbonate-based solutions (as reported in the $2e^-$ WOR literature — see Table S8, Supporting Information). c) Concentration of electrochemically generated H_2O_2 versus the applied current. d) Appt. H_2O_2 faradaic efficiency of BDD-a in different K_2CO_3/$KHCO_3$ solutions plotted as a function of the applied current. e) Partial current density (left Y axis) and initial (int.) H_2O_2 generation rate (right Y axis) of BDD-a in different K_2CO_3/$KHCO_3$ solutions under the average cell voltage.

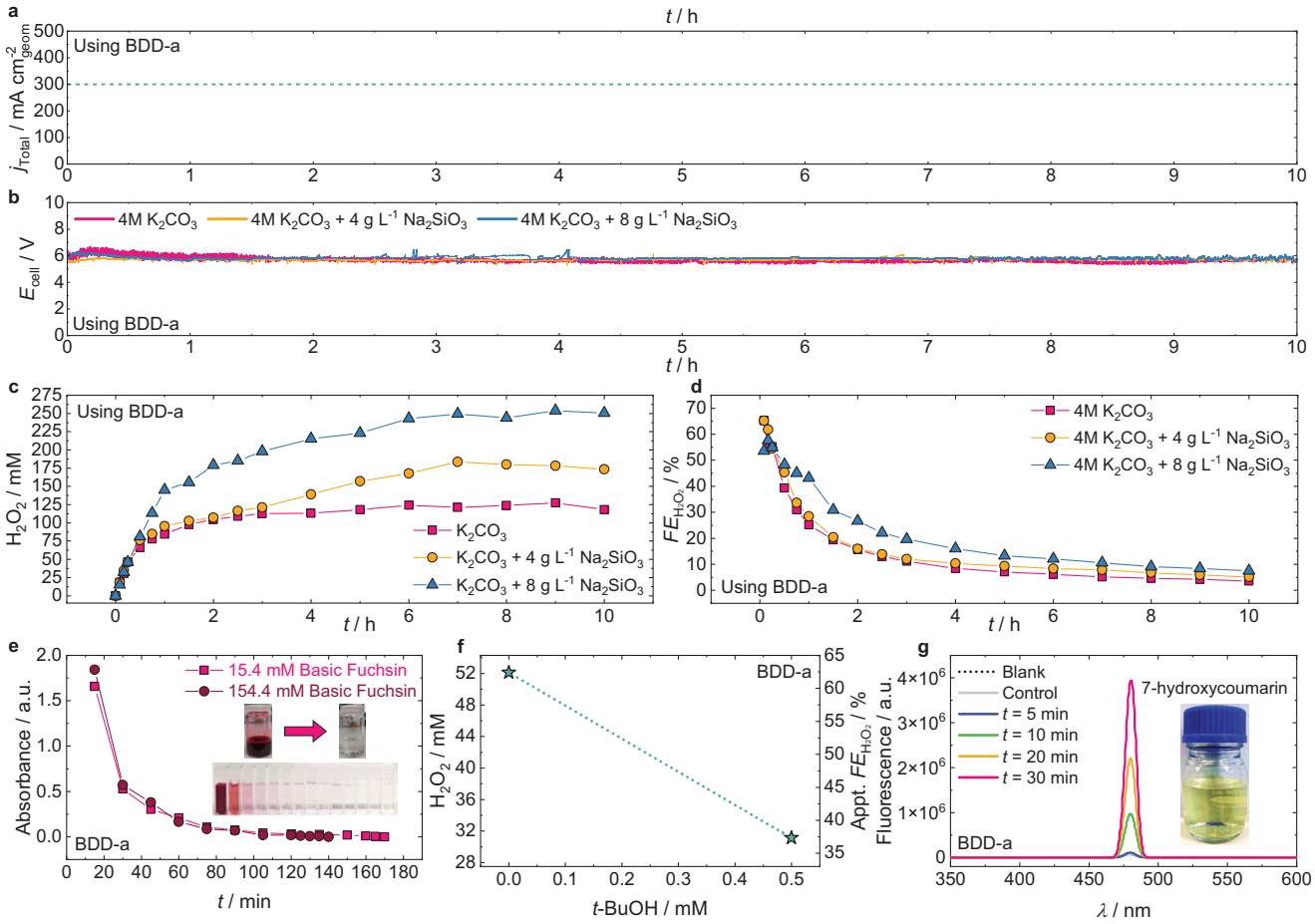

Figure 6. Prolonged electrosynthesis of H_2O_2 via the $2e^-$ WOR using BDD-a in a custom-made flow reactor with an electrolyte flow rate of 400 mL min^{-1}. a) Applied electrical current versus time. b) Total cell voltage of BDD-a recorded in 4 M K_2CO_3 (purple trend), 4 M K_2CO_3 mixed with 4 g L^{-1} Na_2SiO_3 (yellow trend), and 4 M K_2CO_3 mixed with 8 g L^{-1} Na_2SiO_3 (pink trend) plotted as a function of time. c) Accumulation (recirculation) of electrochemically generated H_2O_2 over time using BDD-a in different 4 M K_2CO_3 solutions. d) Appt. H_2O_2 faradaic efficiency as a function of time. e) Absorbance of two different concentrations of basic fuchsine dye (15.4 and 154.4 mM) plotted versus time, as electrochemically generated H_2O_2 (from BDD-a) decolorises the dye. Inset photograph: degradation of concentrated dye over 3 h. f) Electrochemically accumulated H_2O_2 (left Y axis) and H_2O_2 faradaic efficiency (right Y axis) plotted as a function of the concentration of tert-butanol added to the anolyte. g) Photoluminescence spectra collected for BDD-a in 2 M K_2CO_3 with 5 mM of coumarin following a 30 min period of electrolysis. Inset photograph: formation of 7-hydroxycoumarin (yellow-colored solution) during electrolysis.

The electrochemical production of the unrivaled H_2O_2 concentrations (0.94% w/w) for the $2e^-$ WOR attained in this work is further confirmed via the complete decolorisation and degradation of organic dye contaminants (ex. Basic Fuchsine)[38] in deionized water using H_2O_2 samples derived from the 10 h continuous recirculation flow stability test (Figure 6c). The degradation of the dye was quantified by measuring the UV–vis absorbance of the solution as a function of time (Figure 6e). The dye was prepared in two concentrations, 15.4 mM (pink trend) and 154.4 mM (maroon trend) of aqueous Basic Fuchsine. Both dye solutions were promptly degraded upon the addition of H_2O_2. As seen in the inset digital photograph within Figure 6e, the 154.4 mM Basic Fuchsine dye solution turns completely colorless within just 140 min (≈2.3 h), a notably faster decolorization rate compared to the literature,[49] showcasing the impressive oxidizing strength of the electrochemically generated H_2O_2 in this work, under recirculation flow conditions.

The impressive and superior electrocatalytic activity of BDD-a, compared to the other two prepared anodes, BDD-b and BDD-c, can likely be attributed to its larger sp^3/sp^2 carbon ratio, and its rough surface where direct electron transfer can occur due to the formation of a large concentration of hydroxyl radicals (HO•). The HO• radicals, formed via the $1e^-$ WOR, may react with the dissolved inorganic carbon (DIC) species within the carbonate system (CO_3^{2-}/HCO_3^-) of the aqueous supporting electrolyte, resulting in intermediate species (like $CO_3^{\bullet-}$ and HCO_4^-) that upon further oxidation and hydrolysis steps, respectively, promote selective H_2O_2 electrogeneration.[17] The effect of adding tert-butanol, an HO• radical quenching agent,[50] during the electrochemical production of H_2O_2, via water oxidation, in 4 M K_2CO_3, under recirculation flow conditions at an applied current of 300 mA cm^{-2}, is shown in Figure 6f.

The H_2O_2 concentration and appt. *FE* for H_2O_2 production, after 5 min of electrolysis without the presence of the tert-butanol

HO• radical quencher, both reach ≈52 mM and 63%, respectively. Upon the addition of 0.5 M tert-butanol, following 5 min of electrolysis in a fresh solution (4 M K_2CO_3 and 0.5 M tert-butanol), a notable drop in H_2O_2 accumulation and production is observed, with a concentration of just 30 mM determined, alongside an appt. *FE* for H_2O_2 electrosynthesis of 37% (Figure 6f). Consequently, the addition of 0.5 M tert-butanol in the aqueous supporting electrolyte for the $2e^-$ WOR can lead to a 42.3%, for the output H_2O_2 concentration, and 41.3% for the appt. *FE* for H_2O_2 production, drop, respectively, of a BDD-based system, suggesting that electrochemical H_2O_2 generation occurs indirectly via the precursory one-electron formation of the HO• radical.

For the detection of HO• radicals in water, generated at the surface of BDD-a, coumarin, a probe molecule that selectively reacts with HO•, was added to the carbonate supporting electrolyte. Coumarin will react with HO• to form the fluorescent compound 7-hydroxycoumarin that possesses an excitation peak at 477 nm.[51] Thus, in a 2 M K_2CO_3 aqueous supporting electrolyte containing 5 mM of the probe molecule coumarin (100 mL per reservoir; recirculation flow conditions at 400 mL min^{-1}), a constant current density of 300 mA cm^{-2} was applied continuously for 30 min, during which samples were collected at 5, 10, 20 and 30 min, to determine whether the HO• is produced by BDD-a during the $2e^-$ WOR, and detected via coumarin (or specifically, 7-hydroxycoumarin formation), thereby confirming the hypothesis formulated by this research group that the HO• is a key intermediate species for the electrosynthesis of H_2O_2 at the anode. As noted in Figure 6g, after just 5 min of electrolysis in K_2CO_3, BDD-a generated a sufficient amount of HO• detectable at the excitation wavelength of 477 nm (blue line). As electrolysis progresses, the corresponding peaks associated with samples taken at 10 min (green line), 20 min (yellow line) and 30 min (pink line) become larger, thus indicating that a larger concentration of HO• radicals is produced over time, which is directly correlated with the notable increase in the concentration of H_2O_2 (Figure 6c) as a function of the duration of chronopotentiometry under recirculation and galvanostatic flow. This observation provides further support to the theory that, in the BDD/carbonate system assembled within this work for the electrochemical production of H_2O_2 via water oxidation, the formation of H_2O_2 occurs indirectly, likely via the initial electro-generation of HO• radicals from the $1e^-$ WOR.

A more appropriate arrangement for the evaluation of the stability of BDD-a to electrochemically produce H_2O_2 via the $2e^-$ WOR over a prolonged period of time was thus assembled and can be seen in **Figure** 7a. Under single-pass, galvanostatic flow conditions,[52] whereby, for the working electrode (BDD-a) compartment, one reservoir is used to accommodate the anolyte (4 M K_2CO_3) and one reservoir is utilized to collect electro-generated H_2O_2, a constant current density of 300 mA cm^{-2} is applied for 350 h (Figure 7b) at an electrolyte flow rate of 5 mL min^{-1}. Within this setup, BDD-a can maintain a constant cell voltage of 5.5 V at 300 mA cm^{-2} for the entirety of the continuous electrolysis process (Figure 7c), thus exhibiting excellent stability. In contrast to the recirculation flow conditions implemented previously, BDD-a can maintain a constant H_2O_2 output concentration of ≈90 mM (Figure 7d), as well as a stable appt. *FE* of 60% (Figure 7e), for a record 350 h of chronopotentiometry at 300 mA cm^{-2}, accentuating the exceptional capability of BDD-a, the most durable anode for the $2e^-$ WOR designed and investigated to date (Table S8, Supporting Information), to accumulate H_2O_2 at a stable rate over multiple weeks.

2.4. Paired C_2H_4 and H_2O_2 Electro-Synthetic Reactor

The durable and high-performance $12e^-$ CO_2RR cathode and catholyte combination is coupled with the highly active $2e^-$ WOR anode/carbonate system, thus resulting in the assembly of an efficient electrochemical reactor, where the unprecedented parallel paired electrosynthesis of C_2H_4 via CO_2 reduction, and H_2O_2 via water oxidation, at industrially-relevant applied current densities, is realized for the first time. In the separated electrochemical flow cell depicted in **Figure** 8a, our state-of-the-art mixed Cu/Vulcan GDE is employed for CO_2 conversion to C_2H_4 using a 1 M KOH/2 M KI aqueous catholyte, while BDD-a is utilized for H_2O_2 electro-generation via water oxidation in a 4 M K_2CO_3 anolyte. Operated under single pass, galvanostatic continuous flow (electrolyte flow rate: 5 mL min^{-1}; CO_2 flow rate: 0.1–0.2 L min^{-1}) at an optimized applied current density of 200 mA cm^{-2} (Figure 8b), our unique paired $12e^-$ CO_2RR/$2e^-$ WOR cell maintained a stable total cell voltage of ≈5 V for 50 h of constant electrolysis (Figure 8c), exhibiting the excellent compatibility of the two reactions, and stability of the developed anodic, and in particular, cathodic electrocatalysts (Figure S28, Supporting Information). At 200 mA cm^{-2}, our parallel paired electrolysis system achieved an unprecedented combined faradaic efficiency of 120% (*FE*≈60% for the separated $12e^-$ CO_2RR and $2e^-$ WOR, respectively) over 50 h of chronopotentiometry (Figure 8d), which agrees well with the individual half-cell investigations previously carried out in the flow cell and H-type cell (the remaining ~80% electron migration is attributed to the observed thermodynamically-favorable competing O_2, H_2 and CO evolution reactions). The paired $12e^-$ CO_2RR/$2e^-$ WOR reactor also possesses an energy efficiency (EE) of 69%, and a specific energy consumption of 11.77 kWh $kg^{-1}_{Products}$ (mole ratio of 1:6, C_2H_4:H_2O_2), a 50% decrease compared to operating the flow cell using one working electrode (for either C_2H_4, or H_2O_2, production, individually), instead of two as in this instance (Figure S29 and Table S9, Supporting Information). A rudimentary technoeconomic analysis of our new paired $12e^-$ CO_2RR/$2e^-$ WOR electrochemical system further reveals the irrefutable advantage of paired electrolysis, that being a 42% increase in the added value (AV) of the paired electrosynthesis products (1 kg C_2H_4 and 7.05 kg H_2O_2) compared to the non-paired process (Tables S10–S12, Supporting Information). For the most optimistic technoeconomic estimation, where a purchase cost reduction of $\alpha = 5\%$ is utilized (see Experimental Section) for laboratory-scale purchase prices, a positive AV of €0.18 $kg^{-1}_{Products}$ is calculated for the C_2H_4/H_2O_2 electrosynthetic flow reactor compared to a loss of €3.49 $kg^{-1}_{Products}$ for the non-paired electrochemical processes (Figure S30, Supporting Information). Our device thus allows for the efficient and continuous paired, *in situ*, electrosynthesis of C_2H_4, via electrochemical CO_2 conversion, and H_2O_2 from water electrolysis, at large applied electrical currents, with a lower energy cost, and a higher energy efficiency, over an extended period of time.

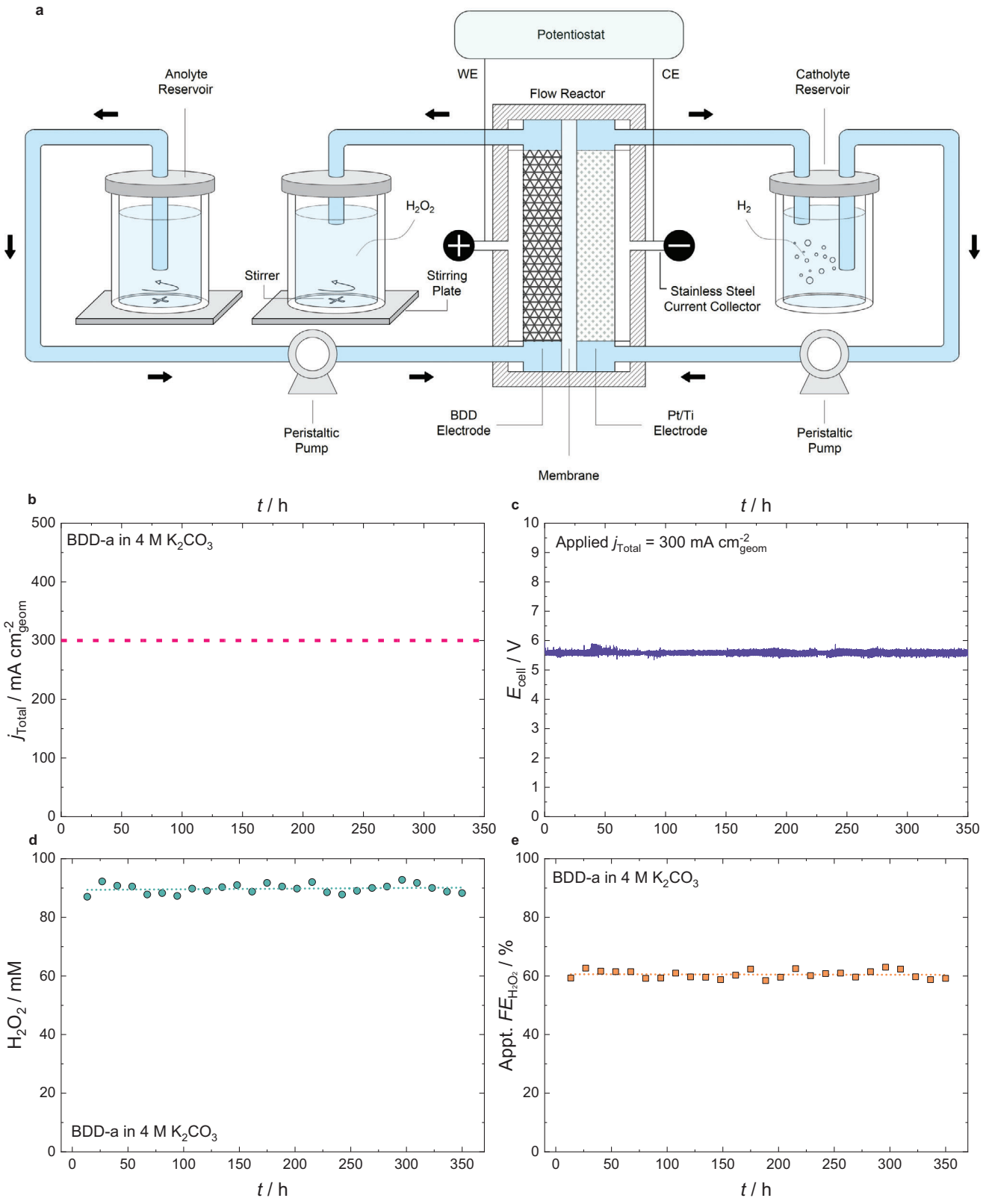

Figure 7. Prolonged H_2O_2 electrosynthesis via the $2e^-$ WOR carried out in an electrochemical flow reactor. a) Schematic diagram of the experimental setup used to electrochemically produce H_2O_2 via water oxidation, using BDD-a, under single pass and galvanostatic flow conditions. b) Applied electrical current versus time. c) Total cell voltage of BDD-a recorded in 4 M K_2CO_3 plotted as a function of time. d) Accumulation (single-pass) of electrochemically generated H_2O_2 over time using BDD-a in 4 M K_2CO_3. e) Appt. H_2O_2 faradaic efficiency as a function of time.

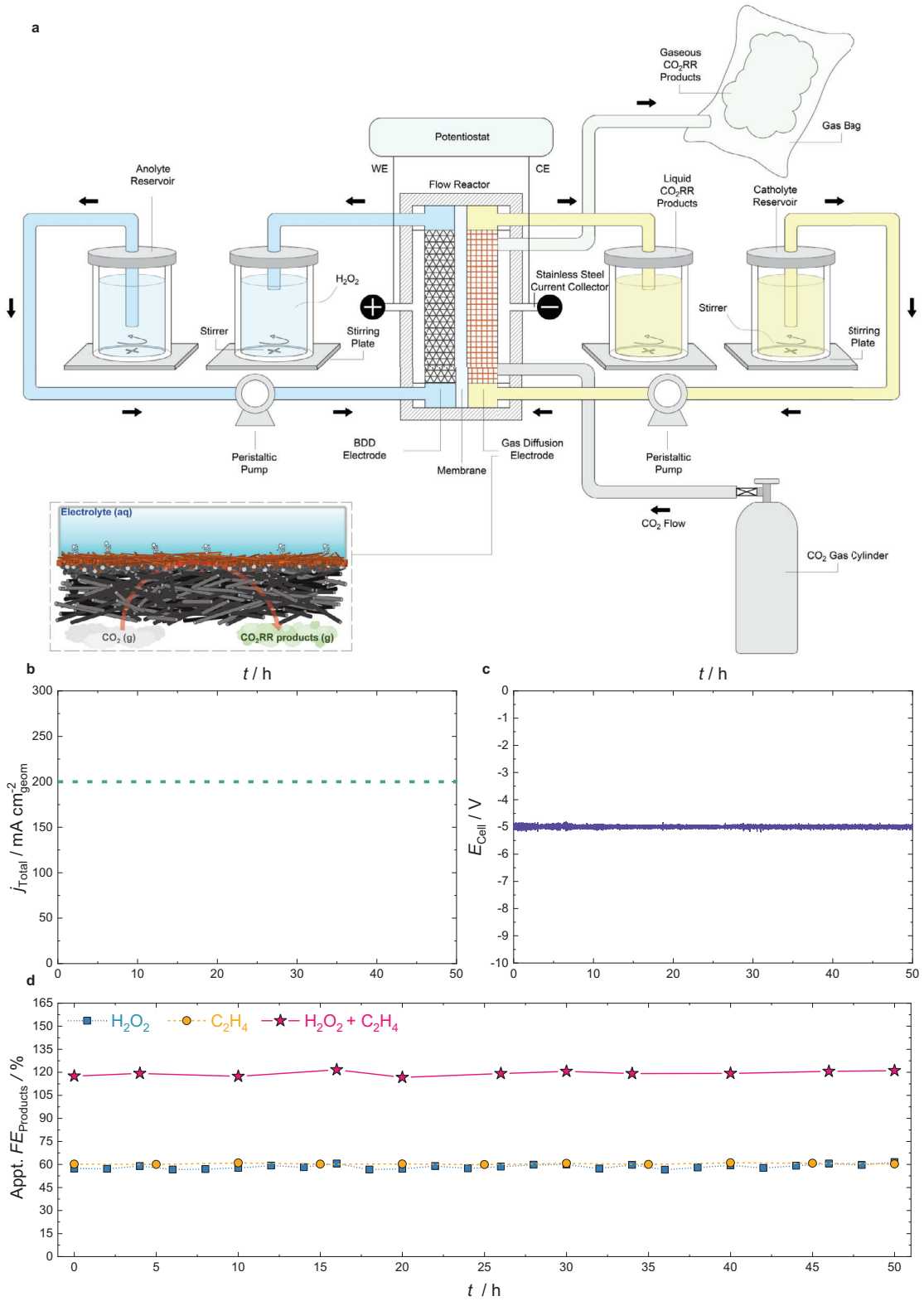

Figure 8. Electrosynthetic reactor for the parallel paired electrosynthesis of C_2H_4 and H_2O_2 via CO_2 reduction and water oxidation. a) Schematic diagram of the experimental setup used to electrochemically produce C_2H_4, via CO_2 reduction using the bespoke mixed-1 GDE, and H_2O_2, via water oxidation using BDD-a, simultaneously in a three-compartment flow reactor, under single pass electrolyte flow conditions, using a single pass of charge. b) Applied electrical current versus time. c) Total cell voltage of the paired C_2H_4-H_2O_2 electrosynthetic reactor plotted as a function of time. d) Appt. H_2O_2 (blue squares), C_2H_4 (yellow circles) and H_2O_2 + C_2H_4 (pink stars) faradaic efficiency as a function of time.

Amongst the most recent paired electrolysis cells assembled within the electrochemical CO_2RR or $2e^-$ WOR/ORR literature, the electro-generation of CO or HCOOH, as well as the convergent paired electrosynthesis of H_2O_2, respectively, have recurrently been reported.[53,54] Our parallel paired C_2H_4/H_2O_2 electro-synthetic reactor is the first, and hitherto only, to couple the $12e^-$ CO_2RR with the $2e^-$ WOR, a combination previously considered to be unfeasible due to perceived limitations associated with the electrocatalytic performance of $2e^-$ WOR catalysts.[55] The results from the measurement depicted in Figure 8 confute this view, as C_2H_4 and H_2O_2 were simultaneously, and uniquely, produced at the largest applied current (200 mA cm^{-2}) using some of the most sizeable (10 cm^2), and the most durable (50 h), electrodes, whilst also delivering the most noteworthy EEC decrease (50%) of the paired electrolysis systems described to date (Table 1).

The dual C_2H_4/H_2O_2 electro-synthetic reactor proposed herein can thus effectuate substantial advancements to CO_2 flow electrolyzers apropos of their overall electrical energy consumption and commercial value.

3. Conclusion

In this work, we sought to address a key bottleneck of contemporary CO_2 flow electrolyzers associated with the wasteful operation of the counter electrode by pairing the electrochemical reduction of CO_2 toward C_2H_4, with the oxidation of water to H_2O_2 in an integrated electrochemical flow reactor. By synthesizing a bespoke mixed Cu nanowire/nanoparticle electrocatalyst loaded onto a Vulcan carbon-based GDL, we first optimized the cathodic reaction, separately, achieving a stable electrocatalytic performance up to 700 mA cm^{-2} and a peak *FE* of 60% for C_2H_4 production, alongside an average cell voltage of 4.2 V, in an engineered KOH/KI catholyte over 370 h of chronopotentiometry at 200 mA cm^{-2}. For water oxidation, our tailored BDD-a coating, grown on niobium, generated H_2O_2 at a maximal concentration of ≈1% w/w in 4 M K_2CO_3/8 g L^{-1} Na_2SiO_3 after 10 h of continuous electrolysis at an industrially relevant 300 mA cm^{-2}, attained a peak H_2O_2 production rate of 135 µmol cm^{-2} min^{-1}, and delivered a stable *FE* of 60% for 350 h of chronopotentiometry at 200 mA cm^{-2} under single pass flow conditions. Consequently, we assembled a unique C_2H_4-H_2O_2 electrosynthetic flow reactor operated under single pass galvanostatic flow conditions to generate the two nexus chemicals at both the anode and cathode, simultaneously, thus maximizing the atom economy and electron utilization of the system and lowering the overall electrical energy consumption of the process. Upon applying 200 mA cm^{-2}, we obtained a stable total cell voltage of 4.99 V over 50 h of continuous dual electrosynthesis and a combined *FE* of 120% for a 1:6 mole ratio of C_2H_4 and H_2O_2, respectively, corresponding to an EE of 69%, and a specific EEC of 11.77 kWh $kg^{-1}_{Products}$, a 50% decrease compared to the EEC of the setup for the individual production of either C_2H_4 or H_2O_2, separately. Additional and advanced research into the functionalisation or modification of the mixed Cu nanowire/nanoparticle catalyst with organic molecules or elements like cerium and iodide may enhance CO-intermediate adsorption on Cu atoms at the surface of the $12e^-$ CO_2RR catalyst, thereby improving selectivity toward C_2H_4, and thus augmenting the current and energy efficiency of our paired electrolysis system. Likewise, for the $2e^-$ WOR, an enriched insight into the precise properties (sp^3/sp^2 ratio, B-doping, crystallite facets) of BDD coatings, loaded on highly-conductive yet cost-effective substrates, that influence superficial $HO^•$ radical generation in carbonate-based aqueous media, will stimulate increased H_2O_2 accumulation over time, thus effectuating improved $FE_{H_2O_2}$ values and minimizing the EEC of the dual C_2H_4/H_2O_2 electrosynthetic reactor. The advancements presented herewithin unlock new research avenues for the large scale, efficient and synchronous electrosynthesis of valuable commodities at both the anode and cathode, with a significantly diminished energy cost, that with further indagation and optimization, may soon compete with mainstream industrial behemoths, such as steam cracking or anthraquinone autooxidation, and render them obsolete.

4. Experimental Section

Chemicals and Materials: All chemicals and reagents utilized in this research were of analytical grade, were used without further purification and were purchased from Merck (Sigma–Aldrich), unless specified. All aqueous electrolytes were prepared daily by dissolving solid powder or pellet precursors (weighed using a Fisherbrand 0.0001 g Analytical Balance) in deionized water (HPLC grade purchased from Sigma–Aldrich or Milli-Q Direct 8 Water Purification System, 18.2 MΩ cm at 25° C). The aqueous electrolytes were stirred for at least 30 min, using a borosilicate-coated magnetic stirring bar, on a hotplate/magnetic stirrer (RCT basic S002 magnetic stirrer) and sealed in Schott glass containers (volume 0.5–1 L) to equilibrate to room temperature. The pH of all the prepared electrolytes was determined using a Jenway 3510 pH meter (pH accuracy ± 0.003 between −2.000 and +19.999), while the specific conductance (or electrolytic conductivity, κ) of the aqueous solutions was measured using a Metrohm 912 Conductometer (± 1% accuracy between 1 and 500 mS cm^{-1}). The primary properties (concentration, pH and conductivity) of the aqueous electrolytes used in the experiments further detailed in this work can be found in Tables S5 and S7 (Supporting Information). All carbon-based gas diffusion layers (GDLs) were purchased from Fuel Cell Store. The niobium (Nb) plates upon which the bespoke boron-doped diamond (BDD) coatings were grown (via hot-filament chemical vapour deposition, HF-CVD) were purchased from Metakem and have a thickness of 1 mm. The Nafion 115 membranes utilized in the electrochemical measurements reported in this research were purchased from Chemours (DuPont).

Electrocatalyst Synthesis: The bespoke mixed copper (Cu) nanowire/nanoparticle catalyst, for the twelve-electron carbon dioxide reduction reaction ($12e^-$ CO_2RR), was synthesized via chemical reflux in which a 500 mL three-necked round bottom flask connected to a water column was supported in a metallic heat jacket (IKA H 135.30 Flask carrier 500 mL without handle), filled with glass wool (Thermo Scientific Chemicals), and placed on top of a hotplate (IKA RCT basic S002). One neck was sealed airtight using sealing grease with a glass stopper, while the remaining neck was used to constantly feed nitrogen (N_2) gas into the system, eliminating any oxygen present that would oxidise the solution and prevent the formation of Cu nanowires/nanoparticles. The water column possessed a glass trap and bubbler on the top vertical outlet (also sealed with grease), which contained oleylamine (technical grade, 70%), thus ensuring a single direction of N_2 flow and further preventing O_2 contamination. A volume of 63 mL of oleylamine was added to the round bottom flask, after which 5.21 g of tri-n-octylphosphine oxide (TOPO, 99%, Thermo Scientific Chemicals) and 0.7754 g of copper (I) bromide (CuBr, 98%, extra pure, Thermo Scientific Chemicals) in a mass ratio of 0.87:0.13, respectively, were immediately added to the solution. The system was flushed continuously with N_2 and was quickly heated to 80° C, where it was constantly stirred for 15 min. Water was then flown through the glass condenser, and the mixture was heated to 260° C and left for 2 h (during this time, the mixture color turns a reddish-brown

Table 1. Reported paired electrolysis systems. Summary of the key operational and performance-related parameters.

Electrolysis Type	Reactions	Electrodes	SA/ cm^2	Cell Type	Products	E_{cell}/V	j/mA cm^{-2}	Combined *FE*/%	t/h	EEC/ kWh $kg^{-1}_{products}$	EEC drop/%	Ref.
Parallel paired	(C) 2e^- CO_2RR and (A) 4e^- $C_3H_8O_2$ OR	(C) Au Plate and (A) Au/C NPs on CC	10	Divided flow cell	(C) CO and (A) LA	2.53–2.63	15	160	2	6.1 (for CO)	35	[56]
Convergent paired	(C) 2e^- CO_2RR and (A) 2e^- OR of CH_3OH	(C) Pt and (A) Pd-B(0.19)/GDL	n/a	Divided H-cell	DMC	1.4 (vs. Ag|AgCl)	~12	83	n/a	n/a	n/a	[57]
Convergent paired	(C) 2e^- ORR and (A) 2e^- WOR	(C) *o*-CNTs and (A) PTFE/CFP-60%	0.42–2	Undivided flow cell	H_2O_2	1.7	120	153	2.5	n/a	n/a	[38]
Convergent paired	(C) 2e^- ORR and (A) 2e^- WOR	(C) TiO_{2-x}/CP and (A) TiO_{2-x}/FTO	1–12	Divided H-cell	H_2O_2	2	3.3–40	134.2	1.1	n/a	n/a	[58]
Convergent paired	(C) 2e^- ORR and (A) 2e^- WOR	(C) ABE-2 and (A) CC/$CuWO_4$/Sn	1	Divided H-cell	H_2O_2	2.9	100	161	2	n/a	n/a	[59]
Convergent paired	(C) 2e^- ORR and (A) 2e^- WOR	(C) *o*-CB and (A) FTO	1–2	Divided H-cell	H_2O_2	2.5	50–100	140	4	n/a	n/a	[39]
Convergent paired	(C) 2e^- CO_2RR and (A) OR of CO + CH_3O^-	(C) Ni SAs/OMMNC and (A) CC	1	Undivided H-cell	DMC	2.9	12	80	1.4	n/a	n/a	[60]
Convergent paired	(C) CO_2RR and (A) AOR	bifunctional $CuCo_2Se_4$/CF	0.283	Divided H-cell	$HCOO^-$ (MeOH) CH_3COO^- (EtOH)	0.7–0.75	50	176.85 ($HCOO^-$) 163.55 (CH_3COO^-)	1	n/a	n/a	[61]
Convergent paired	(C) 2e^- CO_2RR and (A) 8e^- GOR	(C) BiOBr/GDE and (A) Ni_xB	0.95	Divided flow cell	$HCOO^-$	7.67	200	141	2.5	n/a	41	[62]
Convergent paired	(C) 2e^- ORR and (A) 2e^- WOR	(C) NADE and (A) S-CFP	1–4	Divided H-cell	H_2O_2	2.8 (vs. RHE)	70–80	152.9	4	n/a	n/a	[63]
Parallel paired	(C) 2e^- CO_2RR and (A) MeOH OR	(C) Sn-GDE and (A) Pt/Pt_{Ox}	40	Divided flow cell	(C) CH_2O and (A) HCOOH	2.7 – 5	25–75	89	4	n/a	n/a	[64]
Parallel paired	(C) 2e^- CO_2RR and (A) 2e^- WOR	Bifunctional Zn/SnO_2 on CP	n/a	Divided flow cell	(C) $HCOO^-$ and (A) H_2O_2	4.2	~150	158.5	60	n/a	n/a	[65]
Convergent paired	(C) 2e^- CO_2RR and (A) 8e^- GOR	(C) Sn/C GDE (A) Pt or Pt/C	4.5	Divided flow cell	$HCOO^-$	4.4–6.4	50	104	5	n/a	n/a	[66]
Convergent paired	(C) 2e^- ORR and (A) 2e^- WOR	(C) *o*-CNTs and (A) $Ni_{0.13}Ti_{0.87}O_{2-y}$/GDL	1–2	Divided flow cell	H_2O_2	3	120	146	n/a	n/a	n/a	[67]
Linear paired	(C) CH_2O RR and (A) MeOH OR	(C) Carbon black (A) Pt/C or Pt on Ti	1	MEA electrolyser	(A) CH_2O and (C) $C_2H_6O_2$	3.2	100	149	n/a	n/a	n/a	[68]
Parallel paired	(C) 2e^- CO_2RR and (A) FOR	(C) Cu@Sn NWs and (A) MnO_2/CP	0.25–2	Divided H-cell	(C) CO and (A) HCOOH	3.5	4	153.2	6	n/a	47.3	[69]
Parallel paired	(C) 2e^- CO_2RR and (A) SOR	(C) ER-Bi GDE and (A) S-Cu:Co@NF	n/a	Divided flow cell	(C) HCOOH and (A) S_2^{2-}	2.1	100	n/a	8	n/a	40	[70]

(*Continued*)

Table 1. (Continued)

Electrolysis Type	Reactions	Electrodes	SA/ cm^2	Cell Type	Products	E_{cell}/V	j/mA cm^{-2}	Combined *FE*/%	*t*/h	EEC/ kWh $kg^{-1}_{products}$	EEC drop/%	Ref.
Parallel paired	(C) 12e^- CO_2RR and (A) 2e^- WOR	(C) Mixed Cu/GDE and (A) BDD/Nb	10	Divided flow cell	(C) C_2H_4 and (A) H_2O_2	4.99	200	120	50	11.77	50	This work

(C): cathode; (A): anode; CO_2RR: carbon dioxide reduction reaction; OR: oxidation reaction; ORR: oxygen reduction reaction; WOR: water oxidation reaction; AOR: alcohol oxidation reaction; GOR: glycerol oxidation reaction; FOR: formaldehyde oxidation reaction; SOR: sulphide oxidation reaction. Data included in this table derived from literature (excl. this work).

copper color). After exactly 2 h of heating, the system was allowed to naturally cool to room temperature conditions, upon which excess n-hexane (99+%, for analysis, Thermo Scientific Chemicals) was slowly added to the copper-colored mixture. The mixture was then divided into two centrifugal tubes and centrifuged at 4000 rpm for 5 min to remove any unreacted remnants. The resulting Cu precipitate was subsequently washed and centrifuged several times with a 1:1 volume mixture of n-hexane and acetone until the supernate was completely colorless and transparent. A detailed description of the other Cu-based 12e^- CO_2RR catalysts evaluated for ethylene (C_2H_4) electrosynthesis can be found in Figure S31 (Supporting Information). The tailored boron-doped diamond (BDD) coatings for hydrogen peroxide (H_2O_2) electrosynthesis via the two-electron water oxidation reaction (2e^- WOR) were grown on a metallic niobium substrate (Metakem, 1 mm) via hot-filament chemical vapour deposition (HF-CVD) as described in previous studies.[27,48] The primary characteristics of the three BDD anodes utilized in this research have been summarized in Table S1 (Supporting Information).

Gas Diffusion Electrode Preparation: The mixed Cu/Vulcan gas diffusion electrodes (GDEs) used for C_2H_4 electrosynthesis in both the H-cell and flow cell systems presented in this research were prepared via spray deposition of a homogeneous Cu-based catalyst ink onto a Sigracet SGL 28 BC (modified with Vulcan carbon and 40% FEPD 121 filler) gas diffusion layer (GDL, purchased from Fuel Cell Store), denoted in this work as "Vulcan". The homogeneous Cu-based catalyst ink was prepared by mixing the isolated Cu mixed nanowire/nanoparticle solid nanopowder with toluene (99+%, Extra Pure, SLR, Fisher Chemical) in a 1:5 Cu-to-toluene mass ratio, and subsequently sonicating the resulting mixture in an ultrasonic bath (XUBA3, Grant) for 45 min to form a uniform Cu-colored suspension. A suction feed ANCLLO airbrush with a 0.8 mm nozzle was used to deposit the Cu catalyst ink onto the Vulcan GDL via an air compressor (WIZ, Clarke Air) on the 240–250 µm microporous active side. A Vulcan GDL (geometric area of 1.2 × 1.2 cm^2 was used for the H-cell measurements, and an area of 5 × 5 cm^2 was cut for the bulk electrolysis measurements carried out in the flow cell. The airbrush was cleaned prior to, and following deposition, first with deionized water to remove any possible contaminants, and then with isopropanol (IPA, HPLC grade, Fisher Chemical) and n-hexane to sterilise the ink container and the airbrush itself, thus preventing long-term Cu-ink build-up, and possible GDE contamination. The ink was loaded into the cartridge and the airbrush was tested (first with IPA, then will a small amount of the Cu ink) to adjust the level of ink deposition. Upon satisfactory function of the airbrush, the GDL was coated in a circular motion for ≈2 s intervals at a distance of ≈15 cm. Layer overlap was carefully monitored to avoid excessive catalyst deposition, accumulation, and hence potential surface agglomerations, as well as non-uniform (at an eye-level) properties. The GDL sample piece was also rotated by 90° each cycle to ensure the catalyst properly impregnates into the pores within the microporous carbon layer. Spray deposition continued slowly until a catalyst loading of 1 mg cm^{-2} was achieved, with surplus Cu ink prepared to compensate for possible Cu losses during the spraying procedure. After spraying, the resulting Cu-coated GDE was briefly left to dry at room temperature for a minimum of 45 min and was weighed using a precision balance (0.0001 g, Fisherbrand Analytical Balances) to ensure that a catalyst loading of 1 mg cm^{-2} was obtained, prior to electrocatalytic performance testing. A step-by-step illustration of the Cu catalyst synthesis and GDE preparation procedures is presented in Figure S32 (Supporting Information). A graphical illustration of the multiple layers of the mixed Cu/Vulcan GDE for C_2H_4 electrosynthesis from CO_2 reduction is depicted in Figure S33 (Supporting Information).

Materials Characterization: Scanning electron microscopy (SEM) imaging was performed using a FEI Quanta 450 scanning electron microscope and a FEI Helios NanoLab 600i FI DualBeam workstation. High resolution micrographs were obtained via the "immersion mode" setting of the latter device. A Leica EM TIC 3X ion beam milling system was utilized (for 7.5 h at 6 kV) to cut cross-sections of the mixed Cu/GDE cathode and BDD-c anode, thus attaining a sample surface with no detrimental mechanical influences. Transmission electron microscopy (TEM) imaging was performed via a Talos F200i (S)TEM from Thermo Fisher Scientific operated at a primary electron energy of 200 keV and equipped with a

Schottky emitter (X-FEG) alongside a Dual Bruker XFlash 6 | 100 EDS detector. For high-angle annular dark field scanning TEM (HAADF-STEM) and energy dispersive X-ray spectroscopy (STEM-EDXS), a beam current of 40 pA and a convergence angle of 10.5 mrad were both employed. For selected area electron diffraction (SAED), two different selected area apertures of 40 and 200 µm, and a camera length of 840 mm, were used. Laser scanning microscopy (LSM) imaging was achieved using an Olympus LEXT OLS4000 3D laser measuring microscope and the surface roughness of the Cu/GDE and BDD electrode(s) was quantified from line measurements based on ISO 4287-1:1984. X-ray photoelectron spectroscopy (XPS) spectra were recorded using a Physical Electronics 5600 X-ray system equipped with an Al *Kα* monochromatic X-ray source, where the correction was shifted on the carbon peak at 248.8 eV, the take-off angle was 45°, the energy step size was 0.2 eV, and the spot diameter was 800 µm. X-ray diffraction (XRD) analysis of the mixed Cu nanowire/nanoparticle catalyst was carried out using a Malvern Panalytical Empyrean multipurpose diffractometer in Bragg-Brentano (BB) parafocusing geometry alongside a Cu $K\alpha_1$ X-ray source. XRD analysis of the three BDD coatings was completed on a Siemens/Bruker D5000 X-ray powder diffraction system also in Bragg-Brentano (BB) parafocusing geometry alongside a Cu $K\alpha_1$ X-ray source. The peak area for the BDD XRD measurement was assessed by a curve fit on OriginPro. Glow discharge optical emission spectroscopy (GDOES) analysis of the three BDD anodes was implemented to determine the concentration of their respective boron doping using a HORIBA Scientific GD-Profiler 1 calibrated by mass spectrometry standards. Electron Backscatter Diffraction (EBSD) analysis of BDD-c was carried out on the FEI Helios NanoLab 600i FI DualBeam workstation. The Raman spectra of BDD were recorded using a WITec alpha300 R confocal microscope with a 532 nm, 15 mW laser and a grating of 1800 grooves mm^{-1}. Further characterization information of the electrocatalytic materials and supporting substrates utilized in this research can be found in Figures S1–S12, S15, S31, and S33 (Supporting Information).

H-Type Cell Components: Electrochemical screening measurements for the $12e^-$ CO_2RR to produce C_2H_4 were carried out in a custom-made, three-compartment and three-electrode borosilicate H-type glass cell, whereby the cell aperture exposed a 1 cm^2 (geometric) area of the Cu-coated GDE to the aqueous supporting electrolyte. The cell was connected to Metrohm Autolab PGSTAT204 potentiostat equipped with a Booster10A module to increase the maximum current to 10 A. A round PTFE gasket was placed between the working electrode (WE) and the glass flange of the WE compartment to prevent electrolyte leakage. A round and stainless-steel spiral flow field was attached in place behind the WE to introduce CO_2 to the surface of the Cu catalyst, and additionally acted as a current collector. Several layers of parafilm were wrapped around the flow field and glass flange of the WE compartment and secured in place to ensure an air-tight seal. The WE compartment can be filled with ≈75 mL of the aqueous supporting electrolyte. A 25 cm^2 Pt mesh counter electrode (CE) was placed in the CE compartment, (electrolyte volume: 20 mL), which was separated from the WE compartment by a Nafion 115 cation exchange membrane (CEM) previously pre-treated in H_2SO_4. An Hg|HgO (1 M NaOH, RE-61AP, BioLogic) reference electrode (RE) was introduced via a glass Luggin capillary to reduce the distance between the WE and RE and thus minimize the cell resistance. Before any electrolyte was added to either compartment, CO_2 (99.995%, BOC) was allowed to flow through the flow field at a flow rate of 0.1–0.2 L min^{-1} for several minutes ensuring there was suitable pressure behind the GDE. Upon assembling the cell, the CE compartment was filled with electrolyte first, followed by the Luggin capillary and WE compartment in tandem. Upon filling the latter, the cell was tilted at a 30° angle to prevent any possible gaseous bubble accumulation at the surface of the Cu catalyst. A 3D render of the H-type glass cell can be seen in Figure S34 (Supporting Information).

Flow Cell Components and Setup(s): Bulk electrochemical production of C_2H_4 via the $12e^-$ CO_2RR was carried out in a customized three-compartment electrochemical flow cell (Micro Flow Cell, ElectroCell A/S, Denmark), where the working electrode (WE) and counter electrode (CE) compartments were separated by a Nafion 115 cation exchange membrane (CEM), previously pre-treated in 1 M H_2SO_4 and stored in deionized water. A detailed exploded-view diagram of the flow cell and all its components can be seen in Figure S35 (Supporting Information). For the $12e^-$ CO_2RR research reported in this research, the bespoke mixed Cu/Vulcan GDE (Figure S36, Supporting Information) was used as the WE (≈3 × 3.5 cm^2 exposed area; supported on a stainless-steel current collector), while a platinized titanium (Pt/Ti) cathode (≈3 × 3.5 cm^2, Goodfellow Cambridge Ltd) was used as a CE. The flow frames were comprised of PTFE, while the gaskets, used to ensure that the cell was leak-proof, were made of ethylene propylene diene monomer (EPDM). The two endplates were acrylic based. The gas compartment (between Gaskets A and B in Figure S35, Supporting Information) was used to introduce CO_2 (99.995%, BOC) into the system at a flow rate of 0.1–0.2 L min^{-1}, controlled by a precision-machined, acrylic flow meter (FR2000, 0.1–1.0 L min^{-1}, Key Instruments).

A single-pass flow and galvanostatic mode of operation was implemented for C_2H_4 electrochemical generation (Figure S37, Supporting Information). A Metrohm Autolab PGSTAT302N potentiostat, coupled with a Booster20 A, to extend the current range to 20 A, was used to apply electrical current to the cell. A Cole-Palmer Masterflex L/S digital peristaltic pump, equipped with two EASYLOAD pump heads, was used to flow electrolyte (KOH/KI for the 370-h bulk electrosynthesis measurement) through the WE and CE compartments at a flow rate value of precisely 5 mL min^{-1}. The flow cell tubes (Thermo Scientific Nalgene Non-Phthalate Clear Plastic PVC) have an inner diameter (ID) of 3/16 in. and an outer diameter (OD) of 5/16 in. Four thermoregulated borosilicate glass reservoirs (maximum electrolyte volume: 250 mL) were used for single pass flow of the anolyte and catholye (two reservoirs per electrode). The gaseous CO_2RR products electrochemically produced were collected in a 1 L gas sampling bag with a push/pull lock valve (Tedlar, with Thermogreen LB-2 Septa, Merck) for ex situ gas chromatography (GC) analysis.

The two-electron water oxidation reaction ($2e^-$ WOR) screening and bulk electrolysis measurements to electrochemically produce H_2O_2 were carried out in the same ElectroCell flow cell, though it should be noted that the in this instance, the gas compartment is not utilized, and the flow cell is thus operated as a two-compartment reactor. Here, the WE is a boron-doped diamond (supported on niobium, BDD/Nb) anode (≈3 × 3.5 cm^2, custom-made), while the CE in this case is a Pt/Ti cathode (≈3 × 3.5 cm^2). For the recirculation flow measurements, two thermoregulated borosilicate glass reservoirs were used; one for each electrode (Figure S38, Supporting Information). Electrolyte is flown through the system at an average flow rate of 400 mL min^{-1}, following the optimal flow rate identification measurements presented in Figure S26 (Supporting Information). For the single pass flow measurements, two reservoirs were used for the WE (one reservoir to provide the electrolyte to the BDD anode, and one to collect the electrochemically produced H_2O_2), while one reservoir was needed for the CE (where hydrogen evolution is expected to occur) as seen in Figure S39 (Supporting Information). Here, the flow rate of the carbonate-based electrolyte (4 M K_2CO_3) is 5 mL min^{-1}.

Parallel paired electrosynthesis of C_2H_4 via the $12e^-$ CO_2RR and H_2O_2 via the $2e^-$ WOR was also carried out in the customized ElectroCell flow cell in a similar single pass flow setup to the 370-h bulk C_2H_4 electrosynthesis flow cell measurement. The gas compartment was once again utilized for the introduction of CO_2 into the GDE at a flow rate of 0.1–0.2 L min^{-1}, so the cell was operated as a three-compartment flow reactor, essentially comprised of two WEs: the Mixed Cu/Vulcan GDE for C_2H_4 electrosynthesis and BDD-a (coated on Nb) for H_2O_2 electrosynthesis. Single pass and galvanostatic flow conditions were implemented for the dual electrosynthesis experiments in which the electrolyte flow rate was maintained at precisely 10 mL min^{-1}. The anolyte selected is 4 M K_2CO_3, while the catholyte is 1 M KOH/2 M KI. Gaseous CO_2RR products electrochemically produced were once again collected in 1 L gas sampling bags for ex situ GC analysis. The paired C_2H_4-H_2O_2 electrosynthetic flow reactor setup is illustrated in Figure S40 (Supporting Information).

Electrochemical Measurements: In the H-cell, the electrochemical CO_2RR was initiated by applying an electrical current using PGSTAT204 potentiostat coupled with the 10 A booster module. A typical screening experiment was carried out under chronopotentiometry batch conditions at a current density range of 50–300 mA cm^{-2} in 1 M KOH solution (unless otherwise specified). The current was increased in increments of 50 mA cm^{-2}.

Chronopotentiometry was carried out for 5 min (300 s) at each respective current density value. An Hg|HgO (1 M NaOH) reference electrode is used to measure the electrode potential of the Cu/GDE, due to its increased stability in strong alkaline environments. The electrode potential is expressed versus the reversible hydrogen electrode (RHE) as shown in the following equation:

$$ERHE = EHg|HgO + (0.059 \times pH) + E°Hg|HgO \quad (1)$$

where $E°_{Hg|HgO}$ is 0.140 V (1 M NaOH).

The gaseous products generated during the 5 min CO_2RR screening measurements were collected in six different gas sampling bags (previously flushed with N_2 and subsequently degassed under vacuum) for ex situ GC analysis. Intervals of ≈10 s in which no current was applied was programmed into the potentiostat software (Autolab NOVA) between each 5 min chronopotentiometry to allow for the timely exchange of gas sampling bags. In these screening measurements, the electrolyte was not replaced throughout the entire duration of chronopotentiometry, which lasts just over 30 min. Each 30 min screening measurement was repeated at least three times (three independent measurements) to ensure appropriate reproducibility. Liquid CO_2RR products were not determined as part of this research. The same experimental conditions were utilized for all CO_2RR screening measurements though in certain cases, different GDEs (substrate or Cu catalyst) and various aqueous supporting electrolyte combinations were investigated (Figure 3b–e). For the 2 h continuous CO_2RR measurement carried out in the H-cell using 1 M KOH with the mixed Cu catalyst loaded onto different GDL combinations (Figure 3a), a constant current density value of 150 mA cm^{-2} was applied for 2 h, and gaseous samples were collected every 10 min.

For all flow cell measurements, the electrochemical CO_2RR, WOR, or a combination of both (in the case of paired C_2H_4-H_2O_2 electrosynthesis) were initiated by applying a constant current using a PGSTAT302N potentiostat, coupled with a 20 A booster module. For the CO_2RR screening measurements prior to the 370 h stability test, a constant current range of 100–800 mA cm^{-2} in various aqueous KOH/KI electrolytes was applied (Figure 4b). The current was increased in increments of 100 mA cm^{-2}. Chronopotentiometry was carried out for 5 min (300 s) at each respective current density value. Like the H-cell screening tests, the electrolyte was not replaced throughout the duration of chronopotentiometry. Each screening measurement was repeated at least three times (three independent measurements) to ensure appropriate reproducibility. For the CO_2RR stability measurement (Figure 4c–f) using the mixed Cu/Vulcan GDE in 1 M KOH/2 M KI (electrolyte flow rate: 10 mL min^{-1}) a constant current density of 200 mA cm^{-2} (0.2 A cm^{-2}) was applied continuously for 370 h. The BDD anode screening tests were carried out under recirculation flow conditions (50 mL of 4 M K_2CO_3 per reservoir with an electrolyte flow rate of 400 mL min^{-1}) within an applied current density range of 100–500 mA cm^{-2} (increments of 100 mA cm^{-2} per individual 5 min chronopotentiometry measurement). Fresh electrolyte was used for each individual test at each respective current to accurately quantify the amount of H_2O_2 electrogenerated, which was determined following electrolysis. Each individual measurement was repeated at least three times to ensure appropriate reproducibility of this research. Identical operating conditions were implemented for the electrolyte screening tests using BDD-a showcased in Figure 5b–e, though the applied current range was expanded to 100–1000 mA cm^{-2}, the WE used was BDD-a, and some of the aqueous carbonate/bicarbonate electrolytes evaluated have been inspired by the existing 2e^- WOR literature.[27,71,72] The H_2O_2 recirculation stability test (Figure 6a–d) was carried out by applying a constant current density of 300 mA cm^{-2} for 10 h using BDD-a as the anode. Three different aqueous electrolytes were investigated for H_2O_2 production over time: 4 M K_2CO_3, 4 M K_2CO_3 + 4 g L^{-1} Na_2SiO_3 and 4 M K_2CO_3 + 8 g L^{-1} Na_2SiO_3. In these measurements, an electrolyte volume of 150 mL was used in each reservoir. To quantify the concentration of H_2O_2 accumulated over time, 20 mL H_2O_2 samples were taken at regular intervals from the anolyte reservoir which was immediately replenished with 20 mL of fresh anolyte to maintain the volume constant at 150 mL. For the bulk H_2O_2 electrosynthesis measurement carried out under single-pass flow conditions (Figure 7), a constant current of 300 mA cm^{-2} was applied continuously for 350 h using BDD-a as a WE. Two reservoirs were used for the anode: one to feed 4 M K_2CO_3 into the flow reactor, at an electrolyte flow rate of 5 mL min^{-1}, and one to collect electrochemically synthesized H_2O_2. One reservoir was utilized for the CE, where hydrogen evolution was expected, and ultimately observed to take place. For the paired electrosynthesis of C_2H_4 and H_2O_2, using two WEs (mixed Cu/GDE and BDD-a), a constant current density value of 200 mA cm^{-2} was applied continuously for 50 h under single pass (flow rate: 5 mL min^{-1}) flow conditions (Figure 8). Two reservoirs were used for each electrode compartment. The anolyte used was 4 M K_2CO_3 while the catholyte was 1 M KOH/2 M KI.

Dye Degradation and HO• Quenching/Detection Measurements: Degradation of basic fuchsine (dye content >85%) was carried out in parallel to the 2e^- WOR recirculation (flow rate: 400 mL min^{-1}; electrolyte volume: 150 mL) measurement using BDD-a in 4 M K_2CO_3 containing 8 g L^{-1} Na_2SiO_3 under a constant applied current of 300 mA cm^{-2} for 10 h. The dye was prepared in two concentrations (15.4 mM and 154.4 mM of aqueous basic fuchsine), which were placed in two separate 10 mL glass vials. A couple of drops collected from the H_2O_2-containing reservoir (galvanostatic recirculation flow) were placed in the two dye-containing vials at regular 15 min intervals and the decolorization of the dyes was measured via a Jenway 7315 UV–vis single beam spectrophotometer at a wavelength of 544 nm (Figure 6e).

Hydroxyl radical ($HO^•$) quenching experiments were carried out by adding 0.5 M tert-butanol (EMPLURA) to 4 M K_2CO_3 and oxidising the solution (50 mL) using BDD-a as an anode under recirculation and galvanostatic flow conditions (applied current: 300 mA cm^{-2}; electrolysis duration: 5 min; electrolyte flow rate: 400 mL min^{-1}). The resulting mixture was then analyzed to quantify the amount of H_2O_2 produced and evaluate the influence of the radical quencher (Figure 6f). Each 5 min $HO^•$ quenching measurement was repeated at least three times (three independent measurements) to ensure appropriate reproducibility.

Determination of the electrochemical generation of the $HO^•$ radical was realized by oxidizing 100 mL of 2 M K_2CO_3 containing 5 mM of the probe molecule coumarin (≥ 99%) using BDD-a under recirculation and galvanostatic flow conditions (applied current: 300 mA cm^{-2}; electrolyte flow rate: 400 mL min^{-1}) for 30 min. Samples were collected at 5, 10, 20 and 30 min, to determine whether the $HO^•$ is electrochemically produced by BDD-a during the 2e^- WOR, and detected by coumarin via the formation of the fluorescent compound 7-hydroxycoumarin. Approximately 1 mL of the post-electrolysis sample, that possessed a yellow color following water oxidation using BDD was placed in a cuvette, and the emission spectra was measured between 300 and 650 nm (Figure 6g) in a spectrofluorometer (Shimadzu RF-6000, Model S), at a scan rate of 600 nm min^{-1} (excitation bandwidth: 5 nm; emission bandwidth: 5 nm; sensitivity: auto).

Product Quantification: The gaseous products of electrochemical CO_2 reduction were analyzed *ex situ* via gas sampling bags using a gas chromatographer (Shimadzu GC 2030) equipped with a Porapak Q, 80/100 column possessing thermal conductivity (for carbon monoxide, CO) and flame ionization (for methane, CH_4, and ethylene, C_2H_4) detectors. The sampling time was 5 min following electrolysis. All gaseous species were calibrated in advance using certified-grade (SIP Analytical) standard gases (512 ppm ethylene; 503 ppm ethane; 505 ppm methane; 520 ppm carbon monoxide; 506 ppm hydrogen; balance: carbon dioxide). Liquid CO_2RR products were not quantified as part of this research.

Electrochemically produced H_2O_2, by two-electron water oxidation, was determined by standard potassium permanganate (0.1 N $KMnO_4$, standardised against oxalate, Titripur) titration using 10 mL of sulfuric acid (70% w/w H_2SO_4, Fisher Chemical) as a proton source, diluted in a 1:4 (H_2SO_4:H_2O) ratio. A volume of 20 mL of the H_2O_2-containing sample is added to a 250 mL Erlenmeyer flask, after which a volume of 10–20 mL of diluted H_2SO_4 is added slowly into the flask. The mixture is subsequently titrated slowly using 0.1 N (0.02 M) $KMnO_4$ until a color change was observed at the end point (from an initial colorless state to a very light purple/pink solution). The overall reaction is described based on the following equation:

$$2MnO_{4^-} + 6H^+ + 5H_2O_2 \rightarrow 2Mn^{2+} + 8H_2O + 5O_2 \quad (2)$$

For the 350 h H_2O_2 stability and the paired C_2H_4-H_2O_2 electrosynthesis measurements, semi-quantitative Quantofix Peroxide (1 – 100 mg L^{-1} H_2O_2) test strips and a Quantofix Relax reflectometer were used to initially determine the concentration of H_2O_2, followed by $KMnO_4$ titration.

Faradaic Efficiency Calculation: The spectra derived during GC analysis for each injection of the gaseous CO_2RR products, alongside the applied current density (or charge), the fraction of the electrogenerated gas products and the total volume collected over the duration of electrolysis (typically 5 min), were all utilized to evaluate the CO_2RR performance within this research. The apparent faradaic efficiency (*FE*) for C_2H_4 production was calculated based on the following equation. The same equation is used to calculate the *FE* for CO, CH_4 and H_2 production.

$$\text{FE}\ (\%) = \left(\frac{z \times F \times c \times V}{Q \times (Vm \times 10^6)}\right) \times 100 \quad (3)$$

where z is the number of electrons for C_2H_4 production (12), F is Faraday's constant (96485 C mol^{-1}), c is the concentration of C_2H_4 in ppm, V is the volume of the sampling bag in L, Q is the amount of electric charge passed over 5 min and V_m is 24.15 L mol^{-1} for room temperature and pressure (RTP) conditions.

Upon determining the concentration of H_2O_2 electrochemically produced via water oxidation using BDD, the *FE* for H_2O_2 electrosynthesis using the following equation:

$$\text{FE}\ (\%) = \left(\frac{c \times z \times F \times Q}{i}\right) \times 100 \quad (4)$$

where c is the concentration of electrochemically produced H_2O_2 in M (mol L^{-1}), z is the number of electrons for H_2O_2 electrosynthesis (2), F is Faraday's constant (96485 C mol^{-1}), Q is the electrolyte flow rate (converted to mL s^{-1}) and i is the total applied current (converted to mA).

The *FE* for the paired electrosynthetic reactor is calculated by adding the respective *FE*s of each electrode compartment with a maximum total of 200%.

Electrical Energy Consumption and Energy Efficiency Calculations: The calculation of the electrical energy consumption of the separate and paired electrosynthesis of C_2H_4 and H_2O_2 is based on the two respective chemical reactions, the $12e^-$ CO_2RR and $2e^-$ WOR, expressed below:

$$2CO_2 + 12H^+ + 12e^- \rightarrow C_2H_4 + 4H_2O \quad E^\circ = -1.15\ V\ vs.\ \text{RHE (pH 7)} \quad (5)$$

$$2H_2O \rightarrow H_2O_2 + 2H^+ + 2e^- \quad E^\circ = 1.76\ V\ vs.\ \text{RHE} \quad (6)$$

The number of electrons consumed to electrosynthesize 1 mole of product (z_{Real}) is calculated by dividing the theoretical electron demand ($z_{Theoretical}$) with the *FE* determined from the electrochemical measurements:

$$z\text{Real} = \frac{z\text{Theoretical}}{FE} \quad (7)$$

The electrical energy consumption (EEC), in kWh $kg^{-1}_{Product}$, for both the separate (non-paired) and paired electrosynthesis of C_2H_4 and H_2O_2 is calculated using the following equation:

$$\text{EEC} = \frac{E \times z\text{Real} \times F}{FE \times t} \quad (8)$$

where E is the total cell voltage (V), z is the number of consumed electrons, F is Faraday's constant (96485 C mol^{-1}), *FE* is the faradaic efficiency (%) and t is the time in h.

The energy efficiency (EE) values reported in this study are calculated based on the equation:

$$\text{EE}\ (\%) = \left(\frac{E^\circ}{E}\right) \times FE \quad (9)$$

where E° is the thermodynamic potential for C_2H_4 (−1.15 V vs RHE, at pH 7)[33] and H_2O_2 (1.76 V vs RHE) electrosynthesis, E is the potential/voltage (V) experimentally recorded during CO_2RR and/or WOR electrolysis, and *FE* is the faradaic efficiency (%) for C_2H_4 and/or H_2O_2 production.

Technoeconomic Analysis Calculations: The preliminary technoeconomic evaluation of the non-paired and paired electrochemical processes reported in this work include the utilization of two cost indicators, the capital expenditure (CAPEX), normalised to the lifetime of each respective component, and the operational expenditure (OPEX), accounting for the cost of electricity per kWh, described by the equations below.[56] It is vital to note that for the non-paired processes, all costs refer to the electrochemical production of 1 kg of product (either C_2H_4 or H_2O_2), while the paired process refers to the concurrent electrosynthesis of 1 kg of C_2H_4 and 7.05 kg of H_2O_2 (see Figure S30 and Tables S11 and S12, Supporting Information).

$$\text{CAPEX}\ (€\,kg^{-1}_{Product}) = \frac{\text{Price}_{Anode}}{\text{Lifetime}_{Anode}} + \frac{\text{Price}_{Cathode}}{\text{Lifetime}_{Cathode}} + \frac{\text{Price}_{Reactor}}{\text{Lifetime}_{Reactor}} + \frac{\text{Price}_{Electrolyte}}{\text{Lifetime}_{Electrolyte}} \quad (10)$$

$$\text{OPEX}(€\ kg^{-1}_{Product}) = \text{EEC} \times \text{Cost}_{Electricity} + \text{Cost}_{CO_2} \quad (11)$$

where EEC (kWh $kg^{-1}_{Product}$) is the electrical energy consumption for the separate and paired electrosynthetic processes.

The added value (AV) of the final electrochemically generated chemical commodity is described by the following equation:

$$\text{AV}\ (€\ kg^{-1}_{Product}) = \text{Price}_{Product} - (\text{OPEX} + \text{CAPEX}) \quad (12)$$

where $\text{Price}_{Product}$ (€ $kg^{-1}_{Product}$) is the commercial or market value of the produced chemical (C_2H_4 and/or H_2O_2).

The estimated (techno)economics of scaling up these proposed electrochemical systems on the CAPEX and raw material were further calculated by introducing a reduction factor, α (%), as seen below:

$$\text{AV}\ (€\ kg^{-1}_{Product}) = \text{Price}_{Product} - (\text{EEC} \times \text{Cost}_{Electricity} + \alpha \times \text{Cost}_{CO_2}) - (\alpha \times \text{CAPEX}) \quad (13)$$

Supporting Information

Supporting Information is available from the Wiley Online Library or from the author.

Acknowledgements

This research was financially supported by Schaeffler Technologies AG, and partially funded by the CO_2-based electrosynthesis of ethylene oxide (CO_2EXIDE) project consortium, which received funding from the European Union's Horizon 2020 research and innovation program in cooperation with the sustainable process industry through a resource and energy efficiency (SPIRE) initiative under grant agreement no. 768789. S.M. would like to express his gratitude to Dimitra Georgiadou and Chris Madden, as well as Dean Spasov, all from the University of Southampton, for the fluorescence spectroscopy measurements and 3D rendering of the electrochemical H-type cell, respectively. S.M. and M.N. would like to additionally acknowledge Yuxuan (Xenia) Ma and Rachel McKerracher, both from the University of Southampton, for their assistance with the scanning electron microscope imaging of the various synthesized copper nanopowders. M.G. would like to express his gratitude to the following colleagues for their assistance with the acquisition of data and images related to the characterization of the mixed copper nanocatalyst and boron doped diamond coatings: Luis Morales and Sabine Michel from the Chair of Materials Science and Engineering for Metals at the FAU, Jonas Ihle from the Institute Materials for Electronics and Energy at the FAU, and Hans Schmidt from Neue Materialien Fürth GmbH.

Conflict of Interest

The authors declare that S.R. is a cofounder and shareholder of DiaCCon GmbH, Fuerth.

Author Contributions

S.M. and M.N. contributed equally to this work. S.M., L.W. and C.P.d.L. supervised the project. S.M., M.N. and C.P.d.L. conceived the project and designed the electrochemical experiments. S.M. and M.N. carried out all electrochemical measurements with the assistance of S.E., E.F. and O.B. M.N. and S.M. synthesized the mixed copper catalyst, fabricated the gas diffusion electrodes and engineered the aqueous supporting electrolyte for electrochemical carbon dioxide reduction. M.N., S.E., and O.B. designed and tested the gas diffusion electrodes comprised of different copper catalysts and various carbon-based substrates. M.G., A.K. and A.H. characterized the copper coated gas diffusion electrodes and the boron doped diamond anodes. M.G. and S.R. synthesized the boron doped diamonds coatings. E.F. carried out the prolonged hydrogen peroxide electrolysis measurements, the dye degradation tests and the hydroxyl radical quenching/determination tests and contributed to the analysis of the procured data. A.Z. designed all flow reactor setup schematics, the simplified 3D schematic and exploded view diagram of the flow cell components and the step-by-step graphical illustration of the mixed copper/gas diffusion electrode fabrication process. M.G. carried out the electrical energy consumption, energy efficiency and technoeconomic analysis calculations with the assistance of M.N. M.W., F.D. and P.B. provided the funding and valuable suggestions for this research. S.M. and M.N. analyzed the procured data with the assistance of M.G. and E.F. S.M. and M.N. designed all figures with the assistance of M.G., A.K., A.H. and A.Z. S.M. and M.N. cowrote the manuscript with the assistance of M.G. All authors discussed the results and contributed to the revision of the manuscript.

Data Availability Statement

The data that support the findings of this study are available from the corresponding author upon reasonable request.

Keywords

CO_2 reduction reaction (CO_2RR), ethylene, hydrogen peroxide, paired electrolysis, water oxidation reaction (WOR)

Received: December 9, 2023
Revised: February 2, 2024
Published online: March 14, 2024

[1] M. T. Bender, X. Yuan, K.-S. Choi, *Nat. Commun.* **2020**, *11*, 4594.
[2] H. Sheng, A. N. Janes, R. D. Ross, H. Hofstetter, K. Lee, J. R. Schmidt, S. Jin, *Nat. Catal.* **2022**, *5*, 716.
[3] J. Na, B. Seo, J. Kim, C. W. Lee, H. Lee, Y. J. Hwang, B. K. Min, D. K. Lee, H.-S. Oh, U. Lee, *Nat. Commun.* **2019**, *10*, 5193.
[4] G. Han, G. Li, Y. Sun, *Nat. Catal.* **2023**, *6*, 224.
[5] M. J. Llorente, B. H. Nguyen, C. P. Kubiak, K. D. Moeller, *J. Am. Chem. Soc.* **2016**, *138*, 15110.
[6] J. Sisler, S. Khan, A. H. Ip, M. W. Schreiber, S. A. Jaffer, E. R. Bobicki, C.-T. Dinh, E. H. Sargent, *ACS Energy Lett.* **2021**, *6*, 997.
[7] D. Wakerley, S. Lamaison, J. Wicks, A. Clemens, J. Feaster, D. Corral, S. A. Jaffer, A. Sarkar, M. Fontecave, E. B. Duoss, S. Baker, E. H. Sargent, T. F. Jaramillo, C. Hahn, *Nat. Energy* **2022**, *7*, 130.
[8] W. Zhang, Z. Jin, Z. Chen, *Adv. Sci.* **2022**, *9*, 2105204.
[9] E. W. Lees, B. A. W. Mowbray, F. G. L. Parlane, C. P. Berlinguette, *Nat. Rev. Mater.* **2021**, *7*, 55.
[10] J. Gu, S. Liu, W. Ni, W. Ren, S. Haussener, X. Hu, *Nat. Catal.* **2022**, *5*, 268.
[11] S. Nitopi, E. Bertheussen, S. B. Scott, X. Liu, A. K. Engstfeld, S. Horch, B. Seger, I. E. L. Stephens, K. Chan, C. Hahn, J. K. Nørskov, T. F. Jaramillo, I. Chorkendorff, *Chem. Rev.* **2019**, *119*, 7610.
[12] T. N. Nguyen, C.-T. Dinh, *Chem. Soc. Rev.* **2020**, *49*, 7488.
[13] M. B. Ross, P. De Luna, Y. Li, C.-T. Dinh, D. Kim, P. Yang, E. H. Sargent, *Nat. Catal.* **2019**, *2*, 648.
[14] W. Li, Z. Yin, Z. Gao, G. Wang, Z. Li, F. Wei, X. Wei, H. Peng, X. Hu, L. Xiao, J. Lu, L. Zhuang, *Nat Energy* **2022**, *7*, 835.
[15] A. Ozden, J. Li, S. Kandambeth, X.-Y. Li, S. Liu, O. Shekhah, P. Ou, Y. Z. Finfrock, Y.-K. Wang, T. Alkayyali, F. P. de García Arquer, V. S. Kale, P. M. Bhatt, A. H. Ip, M. Eddaoudi, E. H. Sargent, D. Sinton, *Nat Energy* **2023**, *8*, 179.
[16] S. C. Perry, D. Pangotra, L. Vieira, L.-I. Csepei, V. Sieber, L. Wang, C. Ponce de León, F. C. Walsh, *Nat Rev Chem* **2019**, *3*, 442.
[17] S. Mavrikis, S. C. Perry, P. K. Leung, L. Wang, C. Ponce de León, *ACS Sustain Chem Eng* **2021**, *9*, 76.
[18] C. Xia, J. Y. Kim, H. Wang, *Nat. Catal.* **2020**, *3*, 605.
[19] H. Dotan, A. Landman, S. W. Sheehan, K. D. Malviya, G. E. Shter, D. A. Grave, Z. Arzi, N. Yehudai, M. Halabi, N. Gal, N. Hadari, C. Cohen, A. Rothschild, G. S. Grader, *Nat Energy* **2019**, *4*, 786.
[20] D. Li, J. Yang, J. Lian, J. Yan, *J Energy Chem* **2023**, *77*, 406.
[21] X. V. Medvedeva, J. J. Medvedev, S. W. Tatarchuk, R. M. Choueiri, A. Klinkova, *Green Chem.* **2020**, *22*, 4456.
[22] T. Li, Y. Cao, J. He, C. P. Berlinguette, *ACS Cent. Sci.* **2017**, *3*, 778.
[23] A. R. Rathmell, S. M. Bergin, Y.-L. Hua, Z.-Y. Li, B. J. Wiley, *Adv. Mater.* **2010**, *22*, 3558.
[24] S. Zhao, F. Han, J. Li, X. Meng, W. Huang, D. Cao, G. Zhang, R. Sun, C.-P. Wong, *Small* **2018**, *14*, 1800047.
[25] Y. Li, F. Cui, M. B. Ross, D. Kim, Y. Sun, P. Yang, *Nano Lett.* **2017**, *17*, 1312.
[26] H. Guo, N. Lin, Y. Chen, Z. Wang, Q. Xie, T. Zheng, N. Gao, S. Li, J. Kang, D. Cai, D.-L. Peng, *Sci. Rep.* **2013**, *3*, 2323.
[27] S. Mavrikis, M. Göltz, S. C. Perry, F. Bogdan, P. K. Leung, S. Rosiwal, L. Wang, C. Ponce de León, *ACS Energy Lett.* **2021**, *6*, 2369.
[28] X. Jia, N. Huang, Y. Guo, L. Liu, P. Li, Z. Zhai, B. Yang, Z. Yuan, D. Shi, X. Jiang, *J. Mater. Sci. Technol.* **2018**, *34*, 2398.
[29] Z. Sun, Y. Hu, D. Zhou, M. Sun, S. Wang, W. Chen, *ACS Energy Lett.* **2021**, *6*, 3992.
[30] Z. Zhang, L. Bian, H. Tian, Y. Liu, Y. Bando, Y. Yamauchi, Z.-L. Wang, *Small* **2022**, *18*, 2107450.
[31] C.-T. Dinh, T. Burdyny, M. G. Kibria, A. Seifitokaldani, C. M. Gabardo, F. P. García de Arquer, A. Kiani, J. P. Edwards, P. De Luna, O. S. Bushuyev, C. Zou, R. Quintero-Bermudez, Y. Pang, D. Sinton, E. H. Sargent, *Science* **2018**, *360*, 783.
[32] X. Chen, J. Chen, N. M. Alghoraibi, D. A. Henckel, R. Zhang, U. O. Nwabara, K. E. Madsen, P. J. A. Kenis, S. C. Zimmerman, A. A. Gewirth, *Nat. Catal.* **2020**, *4*, 20.
[33] W. Liu, P. Zhai, A. Li, B. Wei, K. Si, Y. Wei, X. Wang, G. Zhu, Q. Chen, X. Gu, R. Zhang, W. Zhou, Y. Gong, *Nat. Commun.* **2022**, *13*, 1877.
[34] H.-J. Peng, M. T. Tang, J. Halldin Stenlid, X. Liu, F. Abild-Pedersen, *Nat. Commun.* **2022**, *13*, 1399.
[35] W. Ma, S. Xie, T. Liu, Q. Fan, J. Ye, F. Sun, Z. Jiang, Q. Zhang, J. Cheng, Y. Wang, *Nat. Catal.* **2020**, *3*, 478.
[36] Y. Huang, C. W. Ong, B. S. Yeo, *ChemSusChem* **2018**, *11*, 3299.
[37] O. Mynko, I. Amghizar, D. J. Brown, L. Chen, G. B. Marin, R. F. de Alvarenga, D. C. Uslu, J. Dewulf, K. M. Van Geem, *J Clean Prod* **2022**, *362*, 132127.
[38] C. Xia, S. Back, S. Ringe, K. Jiang, F. Chen, X. Sun, S. Siahrostami, K. Chan, H. Wang, *Nat. Catal.* **2020**, *3*, 125.
[39] L. Fan, X. Bai, C. Xia, X. Zhang, X. Zhao, Y. Xia, Z.-Y. Wu, Y. Lu, Y. Liu, H. Wang, *Nat. Commun.* **2022**, *13*, 2668.

[40] T. M. Gill, L. Vallez, X. Zheng, *ACS Energy Lett.* **2021**, *6*, 2854.
[41] X. Shi, S. Siahrostami, G.-L. Li, Y. Zhang, P. Chakthranont, F. Studt, T. F. Jaramillo, X. Zheng, J. K. Nørskov, *Nat. Commun.* **2017**, *8*, 701.
[42] Y. Xue, Y. Wang, Z. Pan, K. Sayama, *Angew. Chem., Int. Ed.* **2021**, *60*, 10469.
[43] X. Shi, S. Back, T. M. Gill, S. Siahrostami, X. Zheng, *Chem* **2021**, *7*, 38.
[44] X. Hu, Z. Sun, G. Mei, X. Zhao, B. Y. Xia, B. You, *Adv. Energy Mater.* **2022**, *12*, 2201466.
[45] J. Baek, Q. Jin, N. S. Johnson, Y. Jiang, R. Ning, A. Mehta, S. Siahrostami, X. Zheng, *Nat. Commun.* **2022**, *13*, 7256.
[46] L. Li, Z. Hu, Y. Kang, S. Cao, L. Xu, L. Yu, L. Zhang, J. C. Yu, *Nat. Commun.* **2023**, *14*, 1890.
[47] D. Pangotra, L.-I. Csepei, A. Roth, C. Ponce de León, V. Sieber, L. Vieira, *Appl. Catal. B* **2022**, *303*, 120848.
[48] S. Mavrikis, M. Göltz, S. Rosiwal, L. Wang, C. Ponce de León, *ACS Appl. Energy Mater.* **2020**, *3*, 3169.
[49] S. Y. Park, H. Abroshan, X. Shi, H. S. Jung, S. Siahrostami, X. Zheng, *ACS Energy Lett.* **2019**, *4*, 352.
[50] W. Yang, Z. Deng, Y. Wang, L. Ma, K. Zhou, L. Liu, Q. Wei, *Sep. Purif. Technol.* **2022**, *293*, 121100.
[51] D. A. García-Osorio, J. Vazquez-Arenas, R. Jaimes, *J. Electrochem. Soc.* **2018**, *165*, J3101.
[52] S. Maljuric, W. Jud, C. O. Kappe, D. Cantillo, *J Flow Chem* **2020**, *10*, 181.
[53] W. Xi, P. Yang, M. Jiang, X. Wang, H. Zhou, J. Duan, M. Ratova, D. Wu, *Appl. Catal. B* **2024**, *341*, 123291.
[54] J. S. Lim, S. H. Joo, *Chem* **2023**, *9*, 2056.
[55] H. Chen, C. Ding, C. Kang, J. Zeng, Y. Li, Y. Li, Y. Li, C. Li, J. He, *Green Chem.* **2023**, *25*, 5320.
[56] E. Pérez-Gallent, S. Turk, R. Latsuzbaia, R. Bhardwaj, A. Anastasopol, F. Sastre-Calabuig, A. C. Garcia, E. Giling, E. Goetheer, *Ind. Eng. Chem. Res.* **2019**, *58*, 6195.
[57] T.-T. Zhuang, D.-H. Nam, Z. Wang, H.-H. Li, C. M. Gabardo, Y. Li, Z.-Q. Liang, J. Li, X.-J. Liu, B. Chen, W. R. Leow, R. Wu, X. Wang, F. Li, Y. Lum, J. Wicks, C. P. O'Brien, T. Peng, A. H. Ip, T.-K. Sham, S.-H. Yu, D. Sinton, E. H. Sargent, *Nat. Commun.* **2019**, *10*, 4807.
[58] K. Dong, J. Liang, Y. Wang, Y. Ren, Z. Xu, H. Zhou, L. Li, Q. Liu, Y. Luo, T. Li, A. M. Asiri, Q. Li, D. Ma, X. Sun, *Chem Catalysis* **2021**, *1*, 1437.
[59] L. Li, L. Xu, A. W. M. Chan, Z. Hu, Y. Wang, J. C. Yu, *Chem. Mater.* **2022**, *34*, 63.
[60] X. Li, S.-G. Han, W. Wu, K. Zhang, B. Chen, S.-H. Zhou, D.-D. Ma, W. Wei, X.-T. Wu, R. Zou, Q.-L. Zhu, *Energy Environ. Sci.* **2022**, *16*, 502.
[61] A. Saxena, S. Kapila, J. E. Medvedeva, M. Nath, *ACS Appl. Mater. Interfaces* **2023**, *15*, 14433.
[62] J. R. C. Junqueira, D. Das, A. Cathrin Brix, S. Dieckhöfer, J. Weidner, X. Wang, J. Shi, W. Schuhmann, *ChemSusChem* **2023**, *16*, 202202349.
[63] C. Ling, A. Liang, C. Li, W. Wang, *J. Zhejiang Univ., Sci., A* **2023**, *24*, 377.
[64] J. Baessler, T. Oliveira, R. Keller, M. Wessling, *ACS Sustain Chem Eng* **2023**, *11*, 6822.
[65] X. Hu, G. Mei, X. Chen, J. Liu, B. Y. Xia, B. You, *Angew. Chem., Int. Ed.* **2023**, *62*, 202304050.
[66] J. Vehrenberg, J. Baessler, A. Decker, R. Keller, M. Wessling, *Electrochem. Commun.* **2023**, *151*, 107497.
[67] Z. Wang, X. Duan, M. G. Sendeku, W. Xu, S. Chen, B. Tian, W. Gao, F. Wang, Y. Kuang, X. Sun, *Chem Catalysis* **2023**, *3*, 100672.
[68] R. Xia, R. Wang, B. Hasa, A. Lee, Y. Liu, X. Ma, F. Jiao, *Nat. Commun.* **2023**, *14*, 4570.
[69] X. Lv, J. Liu, T. Shao, M. Ye, S. Liu, *Catal. Today* **2023**, *420*, 114188.
[70] K. Yang, N. Zhang, J. Yang, Z. Xu, J. Yan, D. Li, S. (F.) Liu, *Appl. Catal. B* **2023**, *332*, 122718.
[71] T. M. Gill, L. Vallez, X. Zheng, *ACS Appl. Energy Mater.* **2021**, *4*, 12429.
[72] S. Mavrikis, M. Göltz, S. Rosiwal, L. Wang, C. Ponce de León, *ChemSusChem* **2022**, *15*, 202102137.